Magnetization Relaxation Processes In Magnetic Thin Films and Multi-Layers

Author:
Yasmin Yeow

Supervisor:
Professor Ong Chong Kim

A Thesis Submitted in Partial Fulfilment for the Requirements for the Degree of Bachelor of Science with Honours

in the

Department of Physics, Faculty of Science
National University of Singapore, 2014/15

April 6, 2015

Abstract

Ferromagnetic thin film samples were created through sputtering before being analyzed using the transmission line technique via Vector Network Analyser and electrical detection via Spin Rectification Effect to identify and quantify magnetization relaxation processes in ferromagnetic thin films. This was achieved by using numerical analyses.

In the first type of thin film, Nickel Iron film with a buffer layer of Iron Cobalt, it was found that the only type of magnetization relaxation process that differentiated the 4 thin film samples was spin pumping.

In the second type of thin film, Ferromagnetic/Antiferromagnetic (Nickel Iron / Manganese Iridium) exchange-biased thin film, the magnetization relaxation processes that differentiated the 7 thin film samples were spin pumping, two-magnon scattering and exchange coupling. It was attempted to quantify the contributions of the different damping processes but this was hampered by the inaccurate Gilbert damping constants obtained, which was due to the presence of two-magnon scattering. However, relations were made to attempt to gauge the relationship between thickness of the Manganese Iridium layer and the amount of spin pumping in a thin film sample. It was also difficult to calculate the exact two-magnon contribution in a thin film sample due to the great number of parameters that needed to be fitted and the randomness of the defects. It was also attempted to estimate the spin hall angle and diffusion length of Manganese Iridium but once again, the task proved challenging due to the inaccurate Gilbert damping constants obtained.

Acknowledgements

To **Professor Ong Chong Kim**, thank you for being my supervisor. Thank you for having enough faith to take me on as your student and for guiding me throughout this entire process. Thank you for encouraging me when I was feeling unsure of myself. I hope that you will be proud of me.

To **Soh Wee Tee**, my unofficial mentor, thank you for putting up with my incessant chattering and my inane questions, without making me feel stupid. Thank you for helping me so much in understanding this project and its execution and for responding to my texts at any time of the day. Most importantly, thank you for all the advice and for being an actual friend to me. I would not have been able to do this without you.

To **Xiaoxi Zhong**, **Sun Weiqiang** and the **rest of the Centre of Superconductivity and Magnetic Materials (CSMM)** lab, thank you for helping me directly or indirectly, whether teaching me how to use a certain equipment or rearranging your schedule to allow me to conduct my experiments or just saying a friendly hi. It was fun being in the same lab as you.

To **my family** and boyfriend, **Chua Teoh Guan**, thank you for being my rocks, for being so understanding when I was stressed and had my bad moods and for being there for me when I wanted to relax. You guys are the most important people to me and I am glad to be able to have gone through this journey with you all by my side every step of the way.

Last but not least, to **my friends**, thank you to half of you for being interested in my project when I explained about my it and the other half for pretending to be. Thank you for all the encouragement and good times.

Contents

List of Figures

List of Tables

Chapter 1

Introduction

In this chapter, I will illustrate the significance of my project and explain the reasons for having undertaken this year-long project.

1.1 Background

Ferromagnetic resonance (FMR) was unknowingly first observed by V. K. Arkad'yev in 1912, when he discovered that iron and nickel wires selectively absorb centimetre radio waves, along with a change in magnetization. He hypothesized that the appearance of absorption bands in the magnetic spectrum was due to the resonance response of elementary carriers of a magnetic moment, which was transferred from the ferromagnetic to applied magnetic field.[1]

In 1923, Ya. G. Dorfman suggested that the optical transitions due to Zeeman splitting could potentially be studied to find out more about the ferromagnetic structure. In 1926, N. S. Akulov sent this field further in the right direction when he brought up the question of the effects of of perpendicular and parallel magnetic fields on the magnetic spectra of ferromagnetism. In 1935, after investigating the effect of resonance and considering ferromagnetic domains, L. D. Landau and E. M. Lifshitz came up with a general theory about how ideal uniaxial ferromagnetic crystals behave when magnetic field is varied. This theory was modified by Kittel in 1947 and is still widely used nowadays.[1, 3]

The first experimental discovery of FMR is by Griffiths in 1946 when he discovered ferromagnetic resonance absorption in pure metals.[2] Since then, interest

in FMR has increased significantly and has been a standard technique used to study properties of magnetic materials in their ground states, especially magnetic anisotropy. FMR has also been successful in measuring magnetic properties up to the submonolayer sensitivity. The FMR technique has since expanded to measure interlayer exchange coupling and magnetization relaxation processes in ultra thin films and superlattices too.[11]

1.2 Motivations

The benefits from using magnetic thin films instead of bulk is evident from the following two equations. Thin films follow Acher's Law, given by [4]

$$(\mu_s - 1)f_{FMR}^2 = (\bar{\mu}4\pi M_s)^2, \tag{1.1}$$

whereas bulk follows Snoek's Law, given by

$$(\mu_s - 1)f_r^2 = (\mu 4\pi M_s). \tag{1.2}$$

where μ_s is the low frequency permeability, f_r is the resonance frequency, f_{FMR} is the ferromagnetic resonant frequency, μ is the magnetic permeability and M_s is the saturation magnetization.

From these two equations, it is evident that thin films can give a higher permeability than bulk can, provided that the same materials and frequencies are used for both thin film and bulk. This shows that thin films can potentially be used for lighter and more compact purposes.

Magnetic thin films have many uses in today's technologically advanced world, especially when it comes to data storage in gadgets such as hard disks. Magnetic thin films, specifically ferromagnetic(FM)/antiferromagnetic(AF) thin films, are already very useful in the field of spintronics and could potentially contribute greatly to the research of high frequency devices based on magnetic thin films.[5]

By experimenting with different types of materials included in the thin films in different configurations using the FMR technique, we can evaluate the damping in that particular thin film, with particular interest in the intrinsic damping,

which is important for attaining high-speed magnetization switching for magnetic random access memory (MRAM) and decreasing the critical current density for spin-transfer-driven magnetic reversal.[6, 7] Therefore, looking into magnetization relaxation processes of different thin films can help with compact applications in data storage.

1.3 Project Objectives

For my project, I will be creating ferromagnetic (FM) thin film samples and analyzing them using the transmission line technique via Vector Network Analyser and electrical detection via Spin Rectification Effect, as well as other numerical analyses, focusing on identifying and quantifying magnetization relaxation processes in FM thin films.

An FM material is made up of domains that align in the direction of the applied magnetic field. Above Curie temperature T_C, spontaneous magentization vanishes and the material becomes paramagnetic. When a microwave magnetic field is applied to a ferromagnetic material, this causes the magnetization in the material to precess around the direction of the static magnetic field. However, when this microwave field is removed, the magnetization relaxes back to the static magnetic field direction.[10]

The types of ferromagnetic thin films that I will be looking at are as follow:
(1) NiFe film with a buffer layer of FeCo
(2) Ferromagnetic(FM)/Antiferromagnetic(AF) (NiFe/MnIr) exchange-biased thin film

The first type will be a ferromagnetic thin film with a buffer layer. For this case, the layer of Nickel Iron (NiFe), also known as permalloy (Py), will be constant at 50nm for all 4 samples, with the buffer layer of Iron Cobalt (FeCo), varying from 0nm to 10nm for the different samples. The second type of ferromagnetic thin film that I will be looking at is an exchange-biased ferromagnetic/antiferromagnetic film. The ferromagnetic material will be NiFe, which will be 50nm for all 7 samples and the antiferromagnetic Manganese Iridium (MnIr) layer will be varied from 0nm to 12nm. Antiferromagnetic materials are materials that have neighbouring spins aligned antiparallel to each other, leading to zero net moment at temperatures below Neel temperature T_N.

Permalloy was a natural choice for the FM layer since it is a soft magnetic material, with a high permeability and low coercivity. Iron Cobalt (FeCo) was chosen as the second FM material as a previous experiment had been conducted in the CSMM lab, with the permalloy layer as the buffer layer.[8] For my project, we attempted to reverse the materials of the FM layers to determine what results we would obtain. In addition, a buffer layer would enhance magnetic properties further. MnIr is an AF material that has a very high Neel temperature, allowing the thin films to have maximum exchange bias. In addition, it exhibits large Spin Hall Effect (SHE).[36] Therefore, having an AF layer also allows the investigation of the effects of exchange bias, as well as to calculate the Spin Hall angle.

Chapter 2

Theory

This chapter illustrates the theoretical concepts necessary to my project. It consists of identifying the different possible magnetization relaxation processes, the Landau-Lifshitz-Gilbert and Kittel equations and exchange bias. The goal of this chapter is to lay the groundwork to understand how certain useful equations come about, which will be used to analyse the raw data, in order to find out about damping in the two different types of thin films.

2.1 Damping in Magnetic Materials

Magnetization relaxation in magnetic materials is due to the damping of uniform precession, though not all the magnetization relaxation processes are present in one magnetic thin film sample. There are many magnetization relaxation processes but they all generally follow three main methods.[10]

2.1.1 Energy Redistribution within the Magnetic System

Energy can be transferred by this method through three relaxation processes though the energy stays within the magnetic system. When energy dissipates from uniform precession to degenerate magnons, the process involved is **two-magnon scattering**. Zero-wavenumber magnons with inhomogeneities are scattered, annihilating the initial magnon and creating a new nonzero-wavenumber magnon that

is degenerate in frequency. The inhomogeneities function as scatterers so as to conserve the total momentum.[10, 13] This is an extrinsic damping process.[18]

When energy is passed from uniform precession to thermal magnons, the process involved could be three-magnon scattering or four-magnon scattering. **Three-magnon scattering** process involves the either the annihilation of two magnons after scattering with each one another and the creation of a new magnon or the annihilation of one magnon and the creation of two new magnons. **Four-magnon scattering** process describes the annihilation of two magnons after scattering with each one another and the creation of two new magnons.[10]

2.1.2 Energy Transfer from the Magnetic System to the Non-Magnetic Systems

Some magnetization relaxation processes are also responsible for the dissipation of energy from the magnetic system to a non-magnetic system. One example of a non-magnetic system will be phonons. The magnetization relaxation process responsible for this is **magnon-phonon scattering**. Energy is transferred from zero-wavenumber magnons to phonons after the two different entities scatter with each other. This process occurs in most magnetic materials.[10]

Another magnetization relaxation is **eddy current**, which involves the transfer of energy of the uniform precession to the lattice through conduction electrons[10]

Other relaxation processes are **charge transfer relaxation**, which is the loss of the energy due to jumping of a 3d electron from an iron ion to another when the magnetic precession results in the breathing of energy levels of each site due to spin-orbit coupling and **slowly relaxing impurity** which involves the loss of energy when the two lowest energy levels split depending on the instantaneous direction of magnetization, causing the rare-earth element impurity to hop from one energy level to another. One last relaxation process that contributes to the transfer of energy from the magnetic system to phonons will be **rapidly relaxing impurity**. The rare-earth element impurities take in energy from precession, causing them to jump from the ground state to an excited state.[10]

Another example of a non-magnetic system is free electrons. One of the magnetization processes accountable for this transfer of energy is **spin-flip magnon-electron scattering**. This process entails the annihilation of a magnon as it

scatters with a free electron, causing the energy to be passed from the electron to the free electron and the spin of the free electron to be flipped. Another possible magnetization process is **breathing Fermi surface**. Magnetization precession modifies the free electron energy states through spin-orbit coupling, leading to the formation of electron-hole pairs near the Fermi level. The energy of electron-hole pairs is transferred to the lattice after scattering with it.[10]

2.1.3 Energy Transfer from the Material to External Systems

When the damping of uniform precession is due to energy passing out of the material and entering the external system, the magnetization relaxation process involved is **spin pumping**. This occurs for materials with a ferromagnet/normal metal interface. Spin current moves from the ferromagnet to the normal metal due to uniform precession, transporting angular spin momentum into the normal metal, causing the spins in the ferromagnetic metal to lose angular momentum and thus, damping to increase.[10, 18] This is an extrinsic damping process since another layer is required to be in contact with the FM material for the FM precession to be damped. However, it has the same form as Gilbert damping, which will be discussed later, and thus, the Gilbert damping constant α is affected by spin pumping.

2.2 Landau-Lifshitz-Gilbert Equation

An electron has a magnetic dipole moment m due to spin, which is given by[12]

$$m = \frac{q\hbar}{2m_e}, \tag{2.1}$$

where q is the electron charge and m_e is the mass of the electron.

The torque τ is the rate of change of spin angular momentum and is given by

$$\vec{\tau} = \frac{d\vec{s}}{d\vec{t}} = \vec{m} \times \vec{H_{eff}}, \tag{2.2}$$

where $\vec{s}$ is the spin angular momentum, $\vec{H_{eff}}$ is the effective magnetic field and gamma is the effective gyromagnetic ratio of the electron given by $\gamma = \frac{m}{s} = \frac{q}{m_e} = 1.759 \times 10^7 \ \frac{abC}{g}$ (C.G.S.)

Therefore, the equation of motion of magnetic dipole moment $\vec{m}$ as it precesses around effective magnetic field $\vec{H_{eff}}$ is[11]

$$\frac{d\vec{m}}{d\vec{t}} = -\gamma \vec{m} \times \vec{H_{eff}}. \tag{2.3}$$

A material is ferromagnetic when all of its magnetic dipole moments $\vec{m}$ positively add to the net magnetization of a ferromagnetic sample $\vec{M}$. At static equilibrium, $\vec{M}$ lies parallel to $\vec{H_{eff}}$. However, when excited by a microwave magnetic field, $\vec{M}$ precesses around $\vec{H_{eff}}$ due to the torque acting on $\vec{M}$ by the $\vec{H_{eff}}$. This can be described by Landau-Lifshitz (LL) equation,[11, 15] which is the combined equation of motion for all the individual magnetic dipole moments $\vec{m}$ and given by

$$\frac{d\vec{M}}{d\vec{t}} = \gamma \vec{M} \times \vec{H_{eff}}. \tag{2.4}$$

When there are magnetization relaxation processes that induce damping, a damping term is introduced in the equation, resulting in the Landau-Lifshitz-Gilbert (LLG) equation [16], which is given by

$$\frac{d\vec{M}}{d\vec{t}} = -\gamma(\vec{M} \times \vec{H_{eff}}) + (\frac{\alpha}{M_s})(\vec{M} \times \frac{d\vec{M}}{d\vec{t}}), \tag{2.5}$$

where α is the dimensionless Gilbert damping constant when it is small. The second term in this equation is the damping term, which acts towards $\vec{H_{eff}}$ and causes $\vec{M}$ to precess inwards as well. The LLG equation can be illustrated in Figure 2.1.

The LLG model can account for many magnetization relaxation processes but it is unable to describe the two-magnon scattering process. Therefore, two-magnon scattering is not accounted for in α, though the presence of two-magnon scattering could cause the value of α to be inaccurate due to the quasi-linear properties and dependence on frequency.

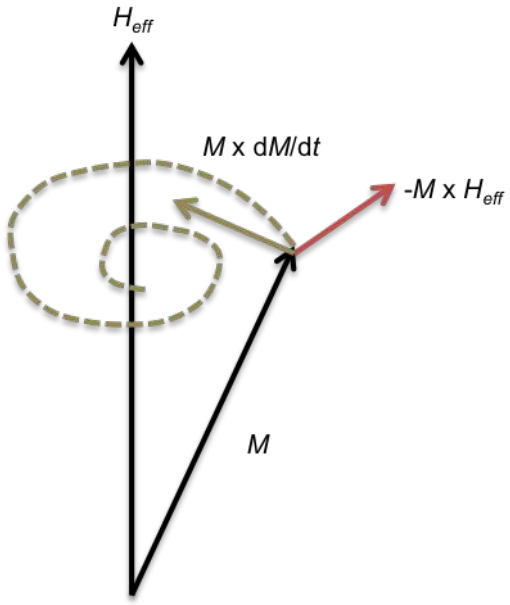

FIGURE 2.1: Precession in a ferromagnet. Figure not drawn to scale.

2.3 Kittel Equation

Considering a cubic ferromagnetic insulator in ellipsoidal form, with principal axes parallel to x, y and z axes in the cartesian coordinate system, the components of the internal magnetic field B in the ellipsoid are related to the applied field H by[14]

$$B_x = H_x - N_x M_x, \tag{2.6}$$

$$B_y = H_y - N_y M_y, \tag{2.7}$$

$$B_z = H_z - N_z M_z. \tag{2.8}$$

For an applied static field $H\hat{z}$, the components from equation 2.4 become[14]

$$\frac{dM_x}{dt} = \gamma(M_y B_z - M_z B_y) = \gamma[H + (N_y - N_z)M]M_y, \tag{2.9}$$

$$\frac{dM_y}{dt} = \gamma[M(-N_x M_x) - M_x(H - N_z M)] = -\gamma[H + (N_x - N_z)M]M_x. \tag{2.10}$$

It is set to $\frac{dM_z}{dt}$=0 and M_z=M to first order. There are solutions with time independence exp($-i\omega t$) only if[14]

$$\begin{vmatrix} i\omega & \gamma[H+(N_y-N_z)M] \\ -\gamma[H+(N_x-N_z)M] & i\omega \end{vmatrix} = 0.$$

Therefore, the ferromagnetic resonance frequency in the applied field H is[14]

$$\omega_0^2 = \gamma^2[H+(N_y-N_z)M][H+(N_x-N_z)M], \tag{2.11}$$

where ω_0 is the ferromagnetic resonance frequency.

For a sphere, where N_x=N_y=N_z, $\omega_0 = \gamma H$.[14]

For a flat plate where H is perpendicular to the plate, N_x=N_y=0 and N_z=4π, resulting in[14]

$$\omega_0 = \gamma(H-4\pi M). \tag{2.12}$$

For a flat plate with H parallel to the plane of the plate, N_x=N_z=0 and N_y=4π, giving[14]

$$\omega_0 = \gamma[H(H+4\pi M)]^{\frac{1}{2}}. \tag{2.13}$$

Equation 2.13 gives us the Kittel equation, which will be used to calculate the parameters of the various thin film samples from the data obtained experimentally.

2.4 Relation to Magnetic Thin Films

For magnetic thin films at room temperature, the FMR linewidth has 3 major contributions

$$\Delta H = \Delta H_{TMS} + \Delta H_{mosaic} + \Delta H_{Gilbert}, \tag{2.14}$$

where ΔH refers to the FMR linewidth signal when full width-half maximum method is used, ΔH_{TMS} is the two-magnon contribution to the linewidth due to two-magnon scattering, which is dependent on frequency, and ΔH_{mosaic} refers to inhomogeneity-caused line broadening, which is independent of frequency.

$\Delta H_{Gilbert}$ is responsible for the intrinsic contribution to FMR linewidth and follows the form $\frac{\alpha\omega}{\gamma}$.

As briefly explained in subsection 2.1.1, two-magnon scattering occurs when zero wavenumber wagons scatter with magnetic defects or inhomogeneities. These inhomogeneities include grain boundaries and surface defects. To conserve momentum, the new magnon created has the same frequency as the initial magnon but a wavenumber k, which is equal in magnitude to the wavenumber of the defect.[10, 13] This process is illustrated by Figure 2.2.

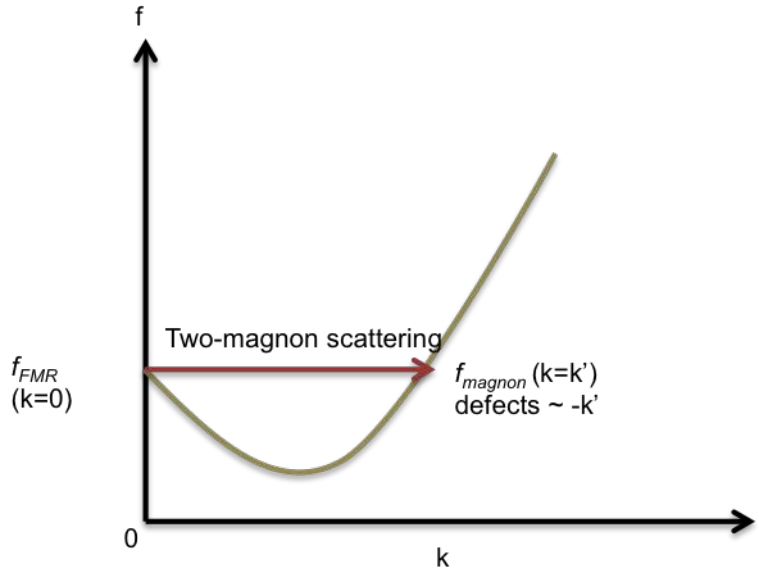

FIGURE 2.2: Two-magnon scattering ΔH_{TMS} process

Using the Arias-Mills formulation,[18, 19] the angular dependence of linewidth H_{TMS} is achieved by introducing an extrinsic-dependent scattering matrix into the spin-wave Hamiltonian, resulting in [13, 20]

$$\begin{aligned}\Delta H_{TMS} = \frac{\rho_0}{(H_Y + H_Z)^2}\{H_Y^2 + [H_Y \cos^2\phi_H + H_Z \cos(2\phi_H)]^2 \times (\langle\frac{a}{c}\rangle - 1) \\ + [H_Y \sin^2\phi_H - H_Z \cos(2\phi_H)]^2 \times (\langle\frac{c}{a}\rangle - 1)\} \sin^{-1}\sqrt{\frac{H_Y}{H_Z}},\end{aligned} \tag{2.15}$$

where ρ_0 represents the strength of the two-magnon scattering along the principal in-plane crystallographic direction and [13]

$$H_Y = H + H_a \cos 2(\phi_H - \eta) + H_{ra} + H_2^{eff}, \tag{2.16}$$

$$H_Z = H + 4\pi M_{eff} + H_a \cos^2(\phi_H - \eta) + H_{ra} + H_1^{eff}, \tag{2.17}$$

where[13]

$$H_1^{eff} = \frac{H_W \cos\phi_{AF}\cos(\phi_H - \phi_{AF} - \beta) - H_e \sin^2(\phi_H - \phi_{AF} - \beta)}{\frac{H_W}{H_e}\cos\phi_{AF} + \cos(\phi_H - \phi_{AF} - \beta)}, \tag{2.18}$$

$$H_2^{eff} = \frac{H_W \cos\phi_{AF}\cos(\phi_H - \phi_{AF} - \beta)}{\frac{H_W}{H_e}\cos\phi_{AF} + \cos(\phi_H - \phi_{AF} - \beta)}. \tag{2.19}$$

H is the strength of the applied magnetic field, H_a is the uniaxial anisotropy field, H_e is the exchange coupling field, H_W is the domain-wall effective field, M_{eff} is the effective magnetization, H_{ra} is the rotatable anisotropy field and ϕ_{AF} is the equilibrium angle of the antiferromagnetic magnetization. In these equations, the easy axes of both the FM and AF layers are assumed to be oriented along the angles η and β respectively, with respect to the direction of the applied magnetic field during growth.[13]

The surface and interface roughness of the thin film samples causes two-magnon scattering due to variation in the surface anisotropy. The defects are supposed to be rectangular-shaped, with height b, lateral dimensions a and c.[13]

ΔH_{mosaic} is not a loss but the superposition of many local FMR shifted profiles for various parts of the thin film sample as shown in Figure 2.3.[10] This could be due to variation in magnetization, internal fields, surface anisotropy, magnetocrystalline anisotropy and film thickness, resulting in small differences in resonance fields for different local FMR profiles.[13]

Due to fluctuations in the uniaxial anisotropy field directions and exchange coupling field strength H_e,[20, 21]

$$\Delta H_{mosaic} = |\frac{\partial H_r}{\partial \eta}\Delta\eta| + |\frac{\partial H_r}{\partial \beta}\Delta\beta| + |\frac{\partial H_r}{\partial H_e}\Delta H_e|, \tag{2.20}$$

where $\Delta\eta$ and $\Delta\beta$ denote the average spread of the direction of the easy axes of the FM and the AF films respectively, H_r represents the resonance field and ΔH_e represents the H_e strength variation at the FM-AF interface.

For my project, the magnetization relaxation processes that I will be looking more into are two-magnon scattering and spin pumping.

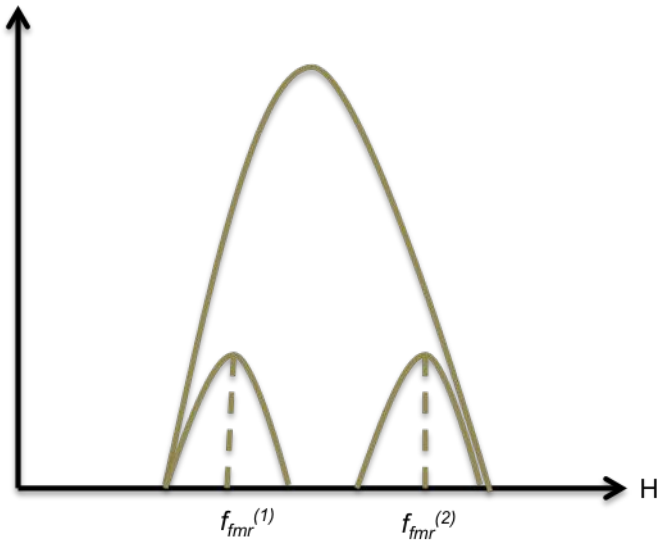

FIGURE 2.3: Inhomogeneous broadening ΔH_{mosaic} process

2.5 Exchange Bias

Exchange bias takes place between an ferromagnetic (FM) and antiferromagnetic (AF) layer. Due to the exchange bias coupling between the FM and AF layer, the AF layer "pins" a certain thickness of the interfacial FM layer, with the rest of the FM layer free to rotate in the magnetic field. An FM hysteresis loop is symmetrical about the origin, suggesting two equivalent favoured directions, along easy axis. Easy axis is the direction inside a crystal, which only requires a small applied magnetic field to reach saturation magnetization. Hard axis, on the other hand, is the direction inside a crystal, which needs a large magnetic field applied in that direction to reach saturation magnetization.[13]

However, when the AF layer is grown on the FM layer in the presence of an external magnetic field, the hysteresis loop, also known as a magnetization-applied magnetic field (M-H) loop, is shifted, indicating a preferred easy magnetization direction for the FM layer. This is the direction that the FM spins are pinned by the AF layer. The shift in the hysteresis loop is shown in Figure 2.4, where the hysteresis loop now has an exchange bias field and an increase in coercivity H_c, relative to an FM hysteresis loop.[22, 23]

According to a model proposed by Stiles and McMichael, the presence of grains that are large enough to stabilize AF order results in the existence of uniaxial anisotropy.[24] When the grains are small, the AF magnetization is immobile while

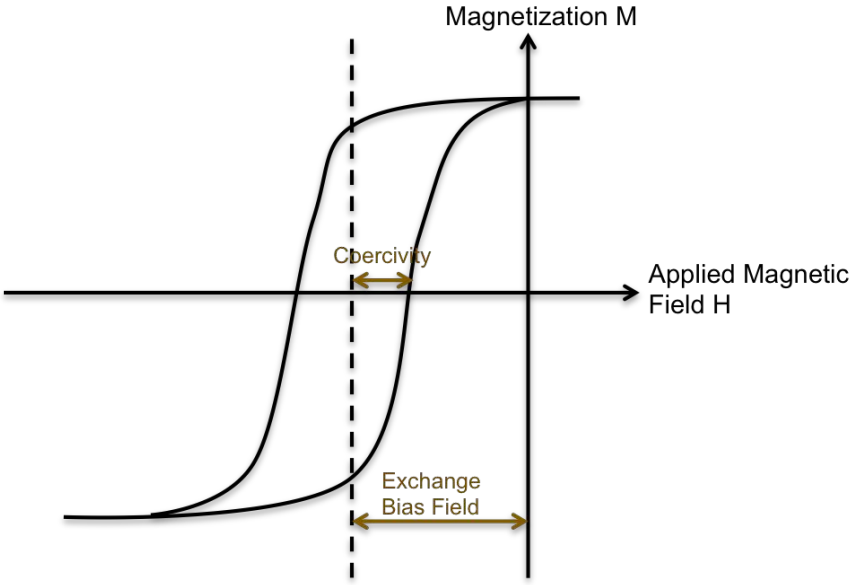

FIGURE 2.4: Hysteresis loop in an exchange-biased thin film sample

the FM magnetization rotates, resulting in hysteretic behavior and the horizontal loop shift in the resonance field during FMR measurements. Thus, the easy axis of these grains is usually set in the FM magnetization direction, resulting in the system being at a lower-energy state.[13]

It has been observed that there is a critical thickness for the AF layer, at which below it, there is no exchange bias, and thus, no exchange bias field H_e given by[32, 33]

$$H_e = \frac{J_E}{M_{FM} t_{FM}}, \tag{2.21}$$

where J_E is the exchange coupling constant, M_{FM} is the magnetization and t_{FM} is the thickness. The reason that there is no exchange bias field below the critical thickness of the AF layer is due to the insufficient AF spins to pin the FM layer. AF grains are freely rotatable and exchange coupled to FM grains. It is also expected that the rotatable anisotropy field H_{ra} is at its peak at the critical thickness. However, once the critical thickness of the AF layer has been passed, exchange bias field sets in and rotatable anisotropy field decreases. This is due to the fact that the thicker the AF layer, the higher the AF domain wall energy and therefore, the more difficult it is to rotate the AF grains.[13]

Chapter 3

Experimental

In this chapter, the general working principles of the different equipment used in this project will be explained. The radio-frequency sputter-deposition system was first used to create the magnetic thin film samples. The MH Loop Tracer was then used to conduct a quick check if the thin film samples were usable and to find out the entropy of each sample. The magnetic thin films were then analyzed using the transmission line technique via Vector Network Analyzer and electrical detection via Spin Rectification Effect.

3.1 Sputtering

The thin film can be created by the use of sputtering. The depositing of a thin film of material onto a substrate or another thin layer of material is called thin film deposition. The thin film deposition process can be split into three categories: thermal evaporation, cathodic sputtering and chemical deposition. The radio-frequency (rf) deposition process falls under cathodic sputtering and is the preferred method by the CSMM laboratory.[25]

The sputtering power source used is of the model ST30-UBQD. The purpose is to support the target and create the RF source for plasma. The RF power generator is of A600RF model, whose purpose is to generate the RF power for the sputtering power source. The RF Auto Tuning and power controller is the model A600MU and regulates the RF power generator and the tuning between the power forward and the reflection power. All three components are manufactured by AJA

International Inc. In figure 3.1 is displayed the sputter-deposition system whereas figure 3.2 shows the inside of the vacuum chamber.

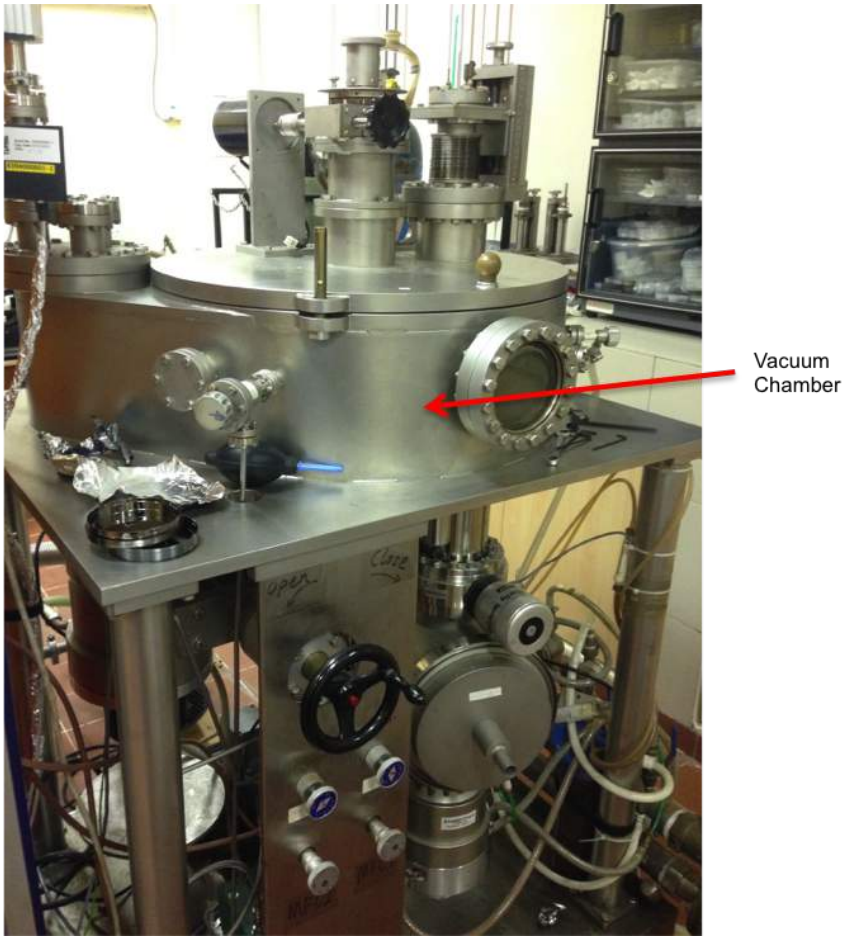

FIGURE 3.1: RF sputter-deposition system

Sputtering is a momentum-transfer process. A radio-frequency sputter-deposition system is used with a base pressure at 7×10^{-7} Torr and ambient temperature in the vacuum chamber. The alloy target is the cathode as it is connected to the negative terminal of an RF power supply. A glow discharge, which is made up of plasma, is maintained between the electrodes. An external magnetic field of 200 Oe was applied during deposition to induce uniaxial anisotropy. The argon pressure was sustained at 2×10^{-3} Torr during the entire deposition process by allowing argon gas to enter the vacuum chamber at a flow rate of 16 SCCM (Standard Cubic Centimeters per Minute).

When positive argon ions collide with the target to eject neutral atoms through the transfer of momentum, this causes atoms from the target material to be ejected and propelled through the plasma towards the grounded Si(100) substrates, which

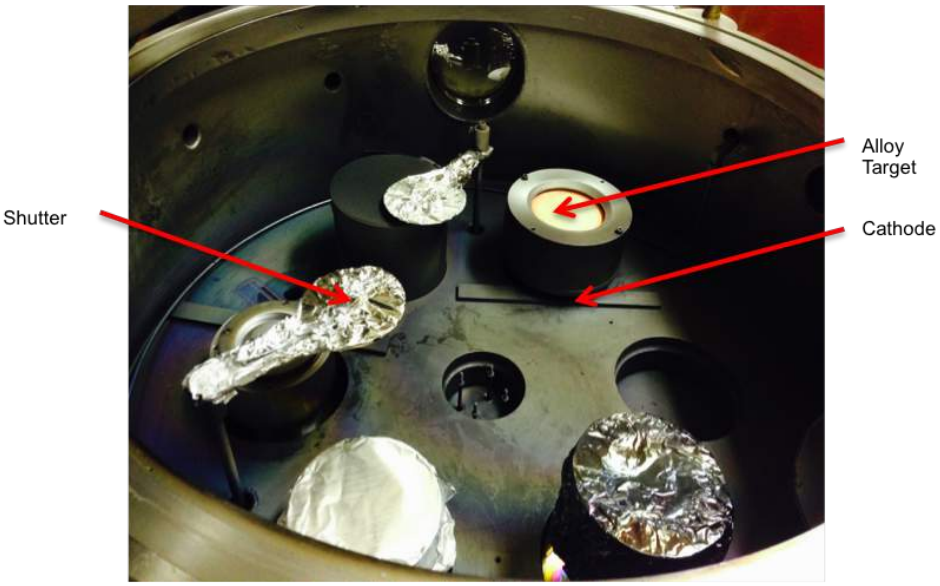

FIGURE 3.2: Inside the vacuum chamber of the RF sputter-deposition system

are facing the alloy targets. The substrates are of length 10 mm, breadth 5 mm and height 0.5 mm. Therefore, a thin film is deposited onto the substrate and held firmly by mechanical forces.[25] When the alloy targets were not being used to sputter into the substrates, they were covered with the shutters.

It should be noted that an AC signal is applied to the electrodes. Above a threshold frequency, two important effects take place. Electrons oscillating in the plasma region acquire enough energy, resulting in ionizing collisions. This reduces the necessity of having secondary electrons to sustain the discharge. Next, RF voltages can be coupled through any impedance. Therefore, it is unnecessary that the electrodes be conductors and any material can be sputtered, regardless of its resistivity.[25]

A huge benefit of this method is that the thickness of material deposited can be easily controlled by coordinating the duration of time that an alloy is sputtered from the alloy sample onto the substrate and by maintaining the deposition rate. [5, 26] Other benefits include a high uniformity of the thickness of the deposited films, good adhesion to the substrate and reproducible thin film samples.[25]

3.1.1 NiFe film with a buffer layer of FeCo

The targets used in this fabrication are 3-inch $Fe_{70}Co_{30}$ and $Ni_{80}Fe_{20}$ alloy targets. While the thickness of the layer of NiFe was maintained at 50 nm for all samples, the thickness of the buffer layer FeCo was varied with the chosen FeCo thicknesses being 0nm, 2.5 nm, 5 nm and 10 nm. This resulted in 4 different thin film samples. The thin films samples were not coated with a layer of SiO_2 so that certain future measurements could be conducted on the samples. Not coating the thin film samples with SiO_2 did not affect the measurements we wished to obtain, as NiFe is relatively resistant to oxidation. An external magnetic field of 200 Oe was applied during deposition to induce uniaxial anisotropy. A thin film sample when the FeCo layer is not 0 nm, is shown in Figure 3.3.

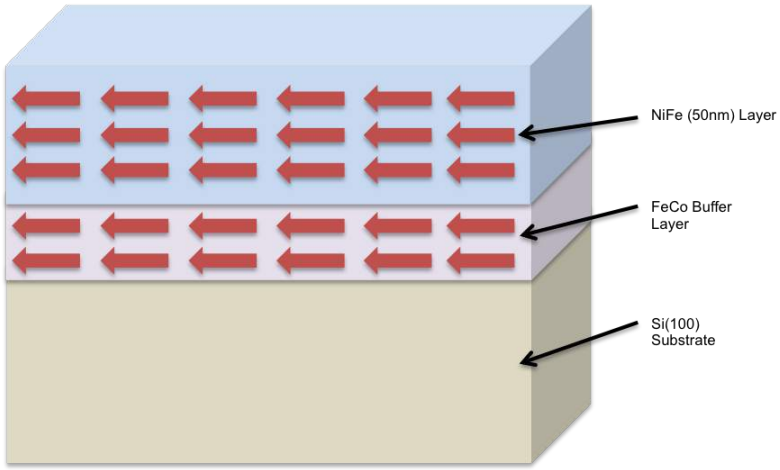

FIGURE 3.3: NiFe(50nm)/FeCo(tnm) thin film sample

3.1.2 Ferromagnetic/Antiferromagnetic (NiFe/MnIr) exchange-biased thin film

The targets used in this fabrication are 3-inch $Mn_{75}Ir_{25}$ and $Ni_{80}Fe_{20}$ alloy targets. For this type of ferromagnetic thin film, the middle portion of the silicon substrates, of about length 6 mm, was covered with paper before being sputtered with copper to form 2 mm-wide copper contacts at opposite ends of the substrate for electrical contact. The copper contacts are higher in height compared to the rest of the thin film sample. The copper contacts were then covered by paper and the middle portion of the substrate uncovered to allow a 50 nm layer of NiFe to be

sputtered onto the substrate. A layer of MnIr was then sputtered onto the NiFe layer. The MnIr layer thickness varied from 0 nm to 12 nm for the 7 samples, with values consisting of 0 nm, 1 nm, 2 nm, 4 nm, 6 nm, 8 nm and 12 nm. Finally, the MnIr layer of each sample was coated with SiO_2 of layer 10nm in situ to protect the samples from oxidation. An external magnetic field of 200 Oe applied during deposition to induce uniaxial anisotropy, was also used to induce external bias here. Figure 3.4 illustrates how a sample should look like when the layer of MnIr is not 0 nm.

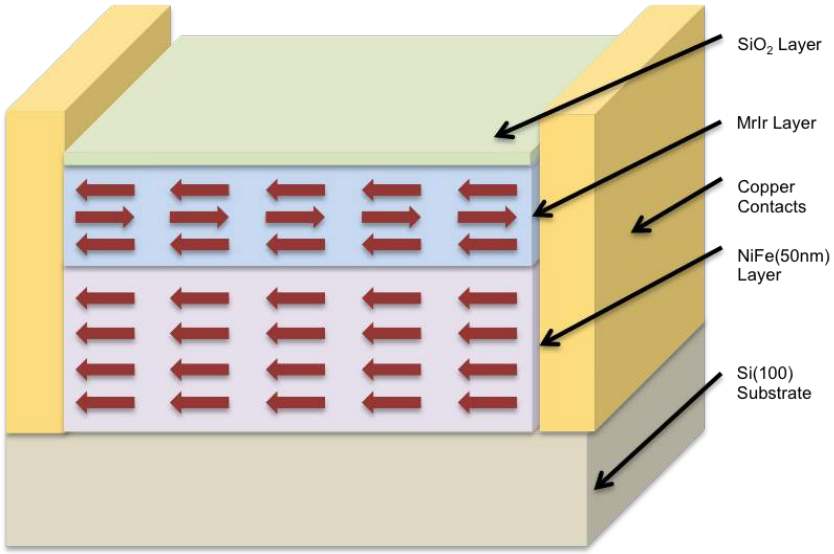

FIGURE 3.4: NiFe(50nm)/MnIr(tnm) thin film sample

3.1.3 Sample Quality

Sample quality was not a problem for my project. The radio-frequency sputter-deposition system used for my project has a very good sputtering base vacuum of 7×10^{-7} Torr whereas the argon pressure is almost 3000 times that. This shows that it is highly unlikely that there will be impurities that will affect the magnetic properties of the thin film samples.

A protective oxide layer, SiO_2, was used to coat the MnIr layer to prevent oxidation. Therefore, even if measurements are conducted on different days, the condition of the thin film samples should not change and the results that we obtain should be largely due to the difference in thicknesses of the buffer layers.

Although the thicknesses of the buffer layers might be small, they are still large enough to ensure that the previous layer is entirely covered by the material sputtered onto it. The spacing between atoms is about 1 to 2 $\times$ 10^{-10} m. Therefore, even the 1 nm MnIr layer has about 5 to 10 monolayers.

The targets used are of high purity standard and they are much larger than the size of the substrate so as to improve the uniformity of the film.

My colleagues at the CSMM laboratory have used the radio-frequency sputter-deposition system numerous times and have used X-ray diffraction to measure the sample quality, as well as a thickness profile meter to measure the thickness. They have yet to experience problems with the sputter-deposition system.[5, 26]

3.2 Vector Network Analyzer

The Vector Network Analyzer (VNA) used in the CSMM lab is of the Agilent Technologies N5230 model. The VNA measures incident, transmitted and reflected energy at high frequencies. While there are two ports on the VNA, we only used one port to measure the phase and amplitude information of the reflected wave, which is then expressed as a vector. The signal generator was responsible for sweeping the thin film sample with microwaves of a range of frequencies. The set-up is shown in Figure 3.5.

Before carrying out measurements, calibration was conducted using the calibration kit. The open port load (Z=∞), short port load (Z=0Ω) and broadband load (Z=50Ω) were fixed to the end of the thick coaxial cable, allowing the VNA receiver to be calibrated to the correct overall wave impedance at different frequencies.

It is necessary to measure FMR for a range of frequencies to find out the intrinsic and extrinsic contributions to FMR linewidth separately.[31] The permeability spectra of the different samples were measured from 10 MHz to 10 GHz, by using a homemade microstrip fixture, as seen in Figure 3.7, and the transmission line perturbation method with the VNA. For the CSMM setup, an external in-plane magnetic field was applied using a Helmholtz coil. Permeance of a magnetic thin film is measured. Permeance refers to the average permeability over the cross section of the thin film times the film thickness. Complex permeability of the magnetic thin film can be obtained from its permeance value when the film thickness

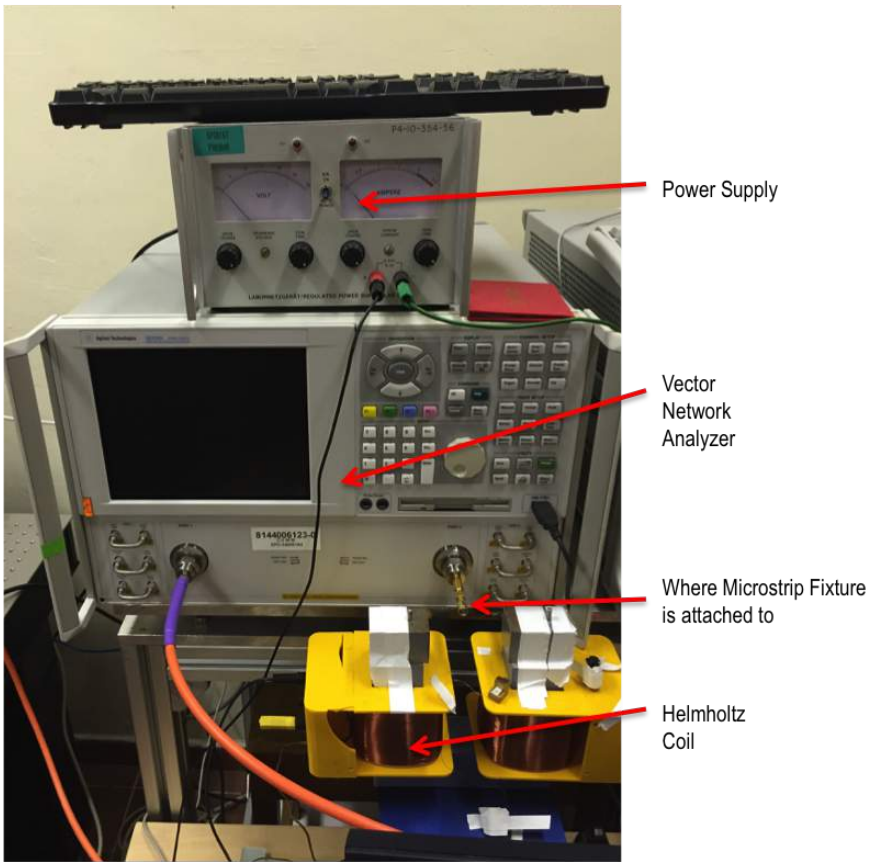

FIGURE 3.5: VNA experimental set-up

is known. From the permeability spectra extracted from the shorted-microstrip measurement, the resonance frequency was obtained from Lorentz fitting of the imaginary permeability spectra.[26]

To obtain the permeability spectra for analysis, some concepts first have to be understood. The VNA makes use of the transmission-line perturbation method. There are two types of transmission line perturbation methods: coaxial line and planar transmission line. For a planar transmission-line perturbation method, the magnetic thin film sample under observation is inserted into a segment of planar transmission line. In doing so, he boundary conditions of the transmission line are changed and thus, the characteristic parameters of the transmission line are changed. From the changes in the transmission-line characteristic parameters, the complex permeability of the thin film can be attained, where it is in the form $\mu_r = \mu_r\prime - j\mu_r\prime\prime$, along with the electromagnetic properties of the magnetic thin film. It should be noted that the propagation mode in the transmission line should not be changed when the sample is inserted.[30]

The characteristic parameters usually used in deriving materials properties are impedance Z, propagation constant γ, effective permittivity ϵ_{eff}, and permeability μ_{eff} where[30]

$$Z = Z_0\sqrt{\frac{\mu_{eff}}{\epsilon_{eff}}}, \tag{3.1}$$

$$\gamma = j\frac{\omega}{c_0}\sqrt{\mu_{eff}\epsilon_{eff}}, \tag{3.2}$$

where Z_0 is the impedance of free space, c_0 is the speed of light in free space, and ω is the angular frequency.

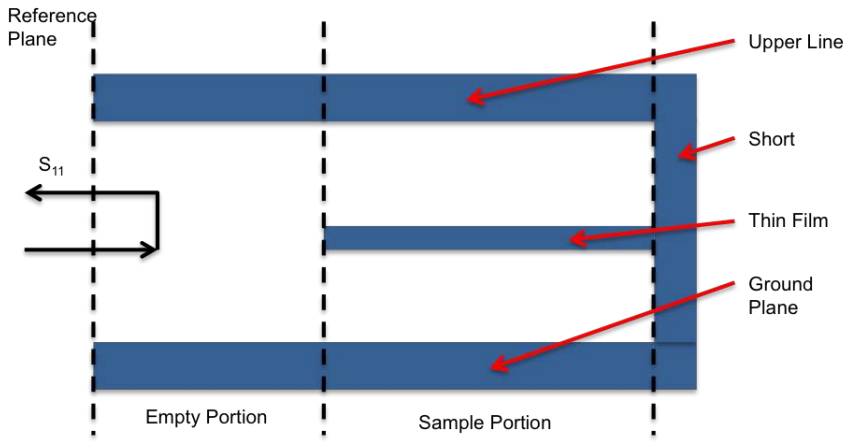

FIGURE 3.6: The reflection approach for characterisation of magnetic thin films

Focusing on the reflection approach as shown in Figure 3.6, the transmission line is short circuited. The magnetic thin film is positioned closely to the shorted end of the transmission line, where magnetic field dominates. Due to the presence of the magnetic thin film sample, the characteristic parameters of the portion filled with the thin film are discontinuous and differ from the characteristic parameters of the empty portion. These discontinuities affect the reflection coefficient S_{11} of the one port used. In addition, the magnetic permeability of the thin film can be obtained from reflection measurements.[27]

In Bekker's model,[27] the complex permeability of a magnetic thin film is calculated from the change in the effective permeability μ_{eff} when the magnetic thin film is inserted. Before the thin film is inserted, $\mu_{eff} = 1$. However, both μ_{eff} and ϵ_{eff} of the transmission line are changed after the insertion of the thin film. At the area where the thin film is positioned, the electric field is perpendicular to the thin film. Due to the small thickness of the thin film, any change of ϵ_{eff} of

the transmission line due to the insertion of the thin film is taken to be negligible. Therefore, since effective permittivity calculated from reflection measurement of the transmission line without the thin film is taken to be the same as the value of effective permittivity of the transmission line loaded with the thin film, μ_{eff} of the transmission line loaded with the thin film can be calculated from the reflection measurement. From the value of the μ_{eff} of the transmission line loaded with the thin film, then the permeability of the thin film can be derived.[30]

The shorted transmission line consists of two portions: the empty portion without thin film and the sample portion where the sample is placed. The ϵ_{eff} of the transmission line before a thin film is inserted can be attained from the reflection coefficient measured at starting point of the transmission line [30]

$$\epsilon_{eff}^{empty}(f) = (\frac{jc_0 \ln[-S_{11}^{empty}(f)]}{4\pi f(l_{empty} + l_{sample})})^2, \tag{3.3}$$

where $S_{11}(f)$ is the reflection coefficient before the insertion of the thin film, l_{empty} is the length of the empty portion, l_{sample} is the length of the sample portion, and f is the measurement frequency. After the thin film is inserted, assuming that the ϵ_{eff} of the transmission line does not change, the effective permeability μ_{eff} of the perturbed transmission line is given by[30]

$$\mu_{eff}(f) = (\frac{jc_0 \ln[-S_{11}^{film}(f)]}{4\pi f l_{sample}\sqrt{\epsilon_{eff}^{empty}(f)}} - \frac{l_{empty}}{l_{sample}})^2, \tag{3.4}$$

where $S_{11}^{film}(f)$ is the reflection coefficient after the thin film sample is inserted. This is the permeability spectra that will be used for further analysis.

3.3 Spin Rectification Effect

The Spin Rectification Effect (SRE) method is to the generation of DC voltages through nonlinear couplings between the microwave excitation fields, spins precession and induced oscillating charge currents[28, 29]

It can be derived from the generalized Ohm's law,[34] which is given by

$$J = \sigma\epsilon_0 - \frac{\sigma\Delta\rho}{M^2}(J \cdot M)M + \sigma R_H J \times H_{eff} + \sigma R_{EH} J \times M, \tag{3.5}$$

where σ is the material's conductivity, $\Delta\rho$ is the change in resistivity due to Anisotropic Magnetoresistance (AMR) and R_H and R_{EH} are the respective ordinary and extraordinary Hall coefficients.

Considering a time-varying current and resistance,

$$I(t) = I_0 \cos(\omega t), \tag{3.6}$$

$$R(t) = R_0 \cos(\omega t + \Phi), \tag{3.7}$$

where I_0 is the initial current, R_0 is the initial resistance, ω is the frequency, t is the time and Φ is the phase difference.

This results in a time-varying voltage given by,

$$\begin{aligned} V(t) &= I_0 R_0 \cos(\omega t)\cos(\omega t + \Phi) \\ &= \frac{1}{2} I_0 R_0 [\cos(2\omega t + \Phi) + \cos(\Phi)], \end{aligned} \tag{3.8}$$

where $\cos(2\omega t + \Phi)$ is the AC component and $\cos(\Phi)$ is the DC component.

The AC component in equation 3.8 will time-average to zero whereas the DC component in the same equation is dependent on the phase.

In a magnetic material, in the absence of electric bias,[17]

$$\vec{V(t)} = \vec{I_{DC}} = -\frac{\sigma\Delta\rho}{M_0^2}[\langle\vec{j}\times\vec{m}\rangle\times\vec{M_0} + \langle\vec{j}\cdot\vec{m}\rangle\vec{M_0}] + \sigma R_H\langle\vec{j}\times\vec{h}\rangle + \sigma R_{EH}\langle\vec{j}\times\vec{m}\rangle, \tag{3.9}$$

where the first, second and third terms are the AMR, Ordinary Hall Effect (OHE) and Anomalous Hall Effect (AHE) respectively.

When

$$\vec{M(t)} = \vec{M_0} + \vec{m(t)}, \tag{3.10}$$

$$\vec{J(t)} = \vec{J_0} + \vec{j(t)}, \tag{3.11}$$

$$\vec{H(t)} = \vec{H_0} + \vec{h(t)}, \tag{3.12}$$

where $\vec{M(t)}$, $\vec{J(t)}$ and $\vec{H(t)}$ are magnetization, current and magnetic field respectively. The oscillating quantities of $\vec{j}$, $\vec{h}$ and $\vec{m}$ couple nonlinearly to produce a DC

voltage from microwave excitation, which is strongly dependent on their relative phases.

SRE measurement is an electrical method, as opposed to the transmission line technique used by the VNA. The configuration used for SRE measurement comprised of a 50 Ω microstrip line to match the test port of the VNA. The space between the upper line and ground plate was left empty so that a thin film sample could be inserted. Therefore, the substrate of the microstrip fixture is air. The width and height of the upper line were chosen to be 5.16 mm and 1.05 mm respectively. The length of the microstrip line in the fixture was chosen to be 9 mm as the length should be less than a quarter wavelength of the highest measurement frequency, which is 4.5 GHz in this case. This is so as to avoid possible resonance in the fixture. The ground plate of the fixture is made of a grounded brass casing, with one side of the microstrip shorted to the casing. The upper line is made from a piece of TMM10i laminate. The TMM10i laminate has a thickness of 0.635 mm, a dielectric constant of 9.8 and a loss tangent of 0.002 at 10 GHz. In addition, it is plated with a layer of copper 37 μm thick, which faces the ground plate in the microstrip fixture.[29, 30] The microstrip fixture can be seen in Figure 3.7.

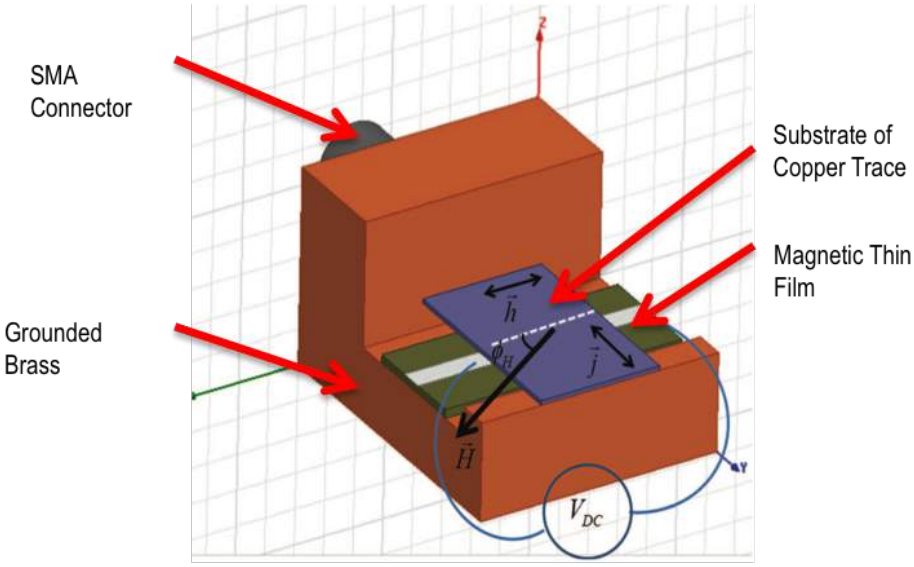

FIGURE 3.7: Homemade SRE Microstrip from reference [29]

Between the line and ground existed an air gap is where the thin film sample can be positioned along the fixture length. The magnetic thin film should be centered between the upper line and the ground plate so as to increase measurement sensitivity. A microwave generator, made up of a SMB100A Rohde and Schwarz

analogue signal generator via SMA (subminiature assembly) connector, will produce $\vec{h}$ in-plane and along the breadth of the microstrip line, the main excitation field for SRE. This is perpendicular to the AC microwave current $\vec{j}$, which is generally along the length of the microstrip line. An in-plane external bias field $\vec{H}$ can be applied once the sample has been inserted, with the help of a Helmholtz coil. The function of a Stanford DS335 function generator is to provide amplitude modulations at 10 kHz, which modifies SRE voltages. These modified SRE voltages are then identified by a Stanford SR830 lock-in amplifier, while power is kept constant at 18dBm.[29] The entire SRE home-made experimental set-up can be seen in Figure 3.8.

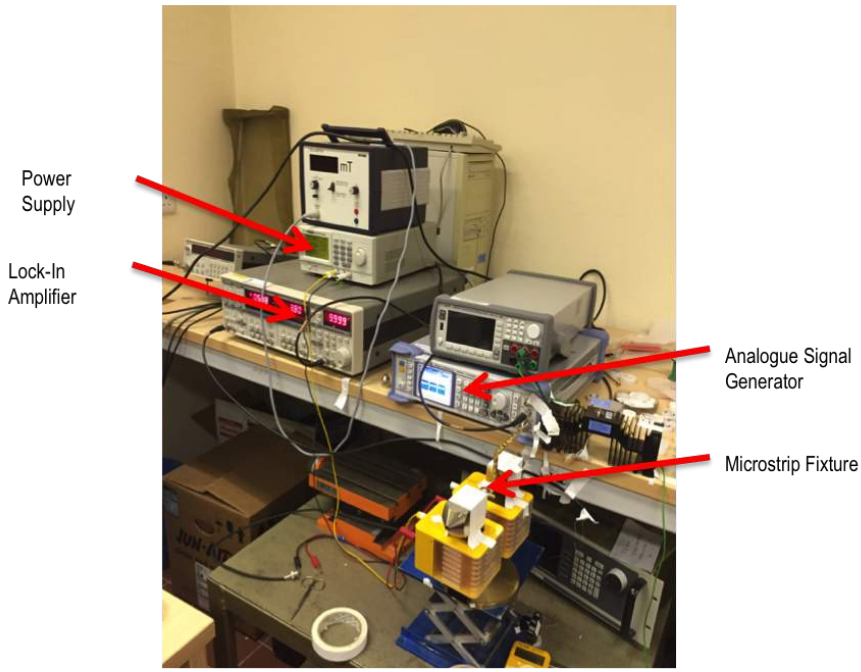

FIGURE 3.8: Home-made SRE set-up

A benefit of this method is that this method is non-destructive as it is unnecessary for the thin film sample to be fused with the microstrip transmission line before sample-microwave coupling occurs, allowing the thin film samples to be used for other measurements. In addition, this method allows for easier sample preparation as lithographic techniques are rendered unnecessary.[29]

There are two types of SRE measurements: angular-dependent and frequency-dependent. However, the sole purpose of these two measurements are the same, which is to determine magnetic properties of thin film samples.

3.3.1 Frequency-Dependent Spin Rectification Effect

For measurement of frequency-dependent SRE, a frequency sweep is carried out from 2 GHz to 4 GHz for the NiFe/FeCo samples and from 2.5 GHz to 4.5 GHz for the NiFe/MnIr samples at a constant power of 18 dBm. For each of the 21 different chosen frequencies, the external magnetic field is swept from 300 Oe to 0 Oe. The voltages of the 21 frequency sweeps were then taken out for further analysis.

3.3.2 Angular-Dependent Spin Rectification Effect

For angular-dependent SRE measurement, the frequency-dependent SRE data was studied. A frequency that has its peak roughly in the middle of the spectrum and that was not too high so as to avoid there being too much background noise, was chosen to be the fixed frequency of about 3 GHz. An SRE measurement was then taken every 10 degrees, between the range of 0 degrees to 350 degrees, with the extreme values included for measurement too. The voltages of the 36 frequency sweeps were then taken out for further analysis.

3.4 Magnetic Hysteresis (MH) Loop Tracer

The Magnetic Hysteresis Loop Tracer used in the CSMM laboratory is made by Hayama Inc. of Japan. The entire MH Loop Tracer set-up is made up of Helmholtz coils, an integral amplifier, a field controller and a computer. After a thin film sample is placed between the Helmholtz coils, the MH loop tracer is operated by applying an AC magnetizing field, generated by the Helmholtz coils, to the sample. The response signal of the sample to the applied magnetic field is then monitored by a pickup coil surrounding the sample. The response signal is sent to the integral amplifier before being sent to an attached computer where the plot of this response results in a hysteresis loop.[25]

The MH loop tracer is used to trace the M-H loops of the samples to conduct a quick check if the thin films were usable after sputtering. This is achieved by checking if there were any horizontal shifts of the M-H loops and if there were, if they were in line with theory or with previous results. Another use of the MH loop

tracer was to find the coercivities of the different thin film samples. The set-up can be seen in Figure 3.9.

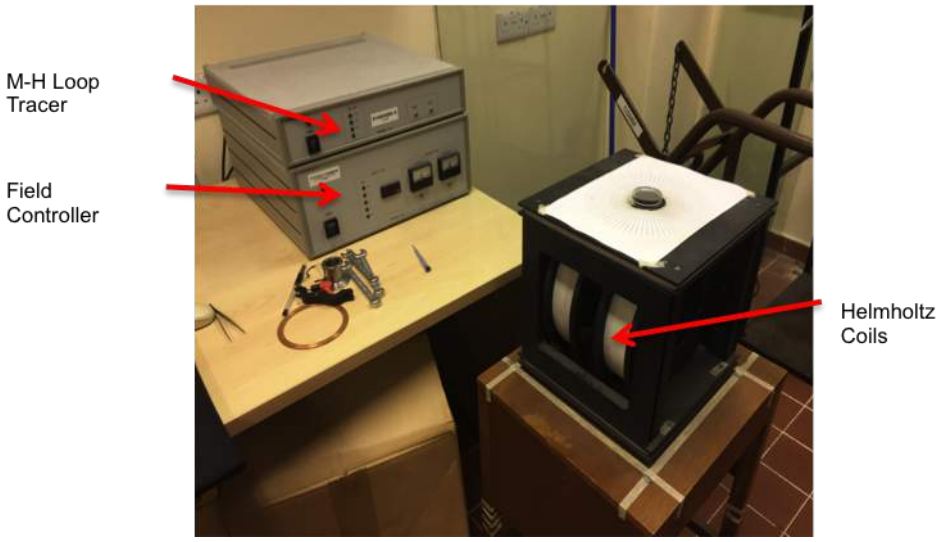

FIGURE 3.9: MH Loop Tracer Set-Up

Chapter 4

Analysis

This chapter focuses on explaining how the data obtained from experimental methods can be analyzed and manipulated to obtain results that we want, related to damping. From this chapter, different parameters and results can be found. However, the parameters that I am most interested in are ΔH_0, α, as well as H_e and H_{ra} to find out the critical thickness and determine the presence of exchange bias. In addition, I am interested in finding the presence of extrinsic damping contribution, the presence of spin pumping, as well as θ_{SHE} and λ_d of MnIr.

4.1 Vector Network Analysis

Only the Lorentzian-shaped, complex component was kept for further calculations. Using OriginPro software by OriginLab, the data points from the curve were fitted to a Lorentz function. The parameters attained from the fitting are the offset of the curve, the FMR frequency ω_0, the full width at half maximum (FWHM) Δf and the area under the curve A. By taking the square of the FMR frequency as the y-axis and the applied field H as the x-axis, the saturation magnetization M_s and uniaxial anisotropy H_k were found from the following equation,

$$\omega_0 = \frac{\gamma}{2\pi}\sqrt{(H + H_k)(H + H_k + 4\pi M_s)}, \tag{4.1}$$

where $\gamma = 1.759 \times 10^7$ and H is the applied magnetic field. Equation 4.1 is adapted from equation 2.13, which is the Kittel equation.

The FWHM Δf values are then converted to ΔH using

$$\Delta H = \frac{\partial H}{\partial f}\Delta f. \tag{4.2}$$

Taking the ΔH values as the y-axis and the FMR frequency as the x-axis, the Gilbert damping constant α and ΔH_0 were attained from equation 4.3, [13]

$$\Delta H = \Delta H_{Gilbert} + \Delta H_0, \tag{4.3}$$

where ΔH represents the peak-to-peak FMR linewidth signal, $\Delta H_{Gilbert} = \frac{2\alpha\omega}{\gamma}$ and [13]

$$\Delta H_0 = \Delta H_{TMS} + \Delta H_{mosaic}, \tag{4.4}$$

4.2 Spin Rectification Effect

4.2.1 Frequency-Dependent Spin Rectification Effect

The magnitude of the voltage was used for further calculations. Using OriginPro, the data points from the magnitude of the voltage were plotted against the applied magnetic field H according to the equation 4.5 [29]

$$V_{DC} = \frac{2A_D\Delta H(H - H_r)}{\Delta H^2 + 4(H - H_r)^2} + \frac{A_L\Delta H^2}{\Delta H^2 + 4(H - H_r)^2} + y_0. \tag{4.5}$$

The parameters gotten for each frequency from equation are A_D which is the magnitude of the dispersive lineshape, A_L is the magnitude of the Lorentzian lineshape, ΔH is the FMR linewidth, H_r is the resonant field and y_0 is the background noise. Equation 4.5 was adapted from equation 3.9.

The values of ΔH are plotted against their respective frequencies according to equation 4.3.

The values of the square of the different frequencies are also fitted to equation 4.1 against their respective H_r values.

4.2.2 Angular-Dependent Spin Rectification Effect

Using OriginPro, the data points from the magnitude of the voltage at each angle ϕ_H were plotted against the applied magnetic field H according to the equation 4.5. The parameters obtained for each angle are A_D which is the magnitude of the dispersive lineshape, A_L is the magnitude of the Lorentzian lineshape, ΔH is the FMR linewidth, H_r is the resonance field and y_0 is the background noise.

The values of H_r were then plotted against their respective angles according to equation 4.6, so as to tell the different components of the magnetic field H.

$$H_r = \sqrt{\frac{\omega^2}{\gamma} - ab + \frac{a+b^2}{2}} - \frac{a+b}{2}, \tag{4.6}$$

where

$$a = H_a \cos(2\phi_H - 180) + H_e \sin\phi_H + H_{ra}, \tag{4.7}$$

$$b = 4\pi M_{eff} - H_a \cos^2(\phi_H) + H_e \sin\phi_H + H_{ra}, \tag{4.8}$$

where H_a is the uniaxial anisotropy field, H_e is the exchange field and H_{ra} is the rotational anisotropy field.

Figure 4.1 displays the directions of H_a, H_e and H_{ra} in a thin film sample.

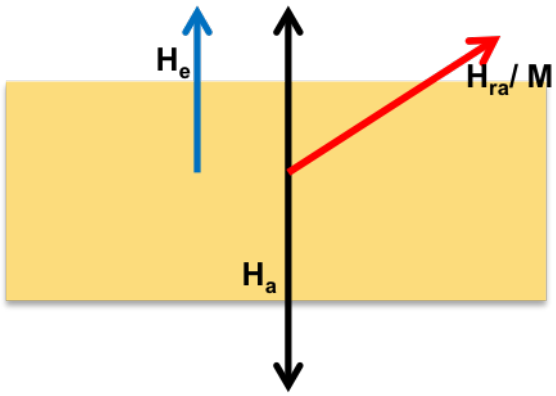

FIGURE 4.1: Directions of H_a, H_e and H_{ra} in a magnetic thin film sample

Next, adapted from equation 4.3,

$$\Delta H = \Delta H_{Gilbert} + \Delta H_{TMS} + \Delta H_{mosaic}. \tag{4.9}$$

While equation 4.9 is essentially equation 4.3, the difference between these two equations is that equation 4.9 is used to fit ΔH values against their respective angles. Since ΔH_{TMS} and ΔH_{mosaic} are dependent on the angle at which frequency is swept, the components of ΔH_{TMS} and ΔH_{mosaic} can be found from equations 2.15 and 2.20 respectively and more parameters can be obtained from equation 4.9 than in equation 4.3.

4.2.3 Using SRE to Measure Inverse Spin Hall Effect (ISHE)

SRE only measures rectified voltages in the FM NiFe and FeCo layers since there is no net magnetization in the AF MnIr layer. Spin current j_s is pumped from the FM layer to the neighbouring layer, causing the FM layer to lose angular momentum and thus, damping increases. This causes a charge current j_c in the FM layer through Inverse Spin Hall Effect (ISHE), which is then converted to give the electric voltage from ISHE contribution. This electric voltage is measured to give V_{ISHE}. This is illustrated in Figure 4.2 where we shall use the NiFe thin film with a buffer layer in the example. For Figure 4.2, although there is spin pumping in both directions since there are two FM layers, only spin pumping from FeCo buffer layer to the NiFe layer is illustrated for easier understanding.[10]

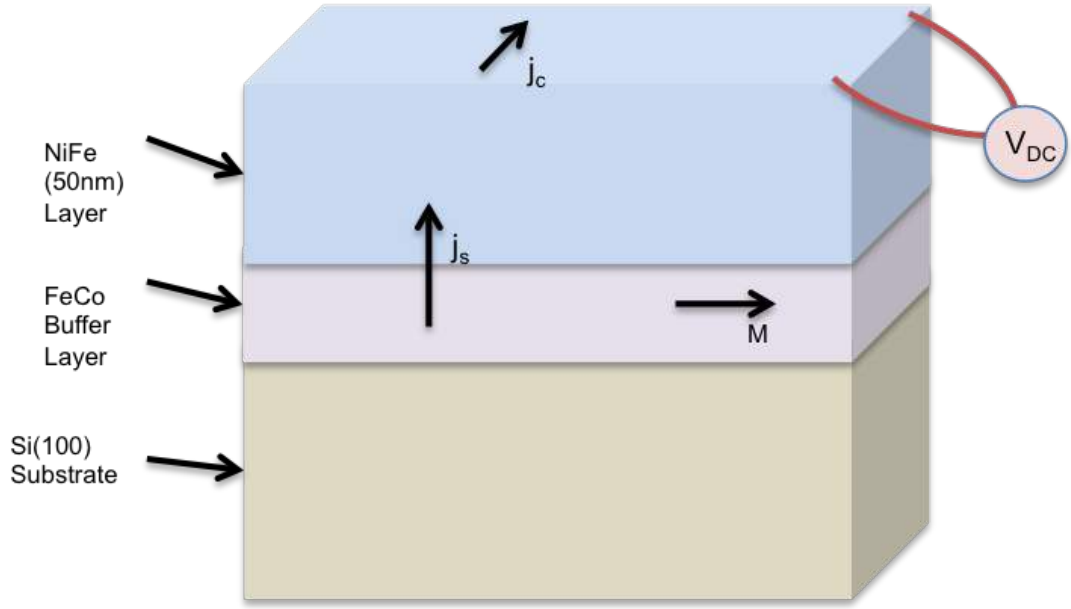

FIGURE 4.2: The directions of j_s, j_c and M in an NiFe(50nm)/FeCo($t$nm) sample. Figure not drawn to scale.

From Figure 4.2,[34]

$$j_c = \frac{2e}{h}\theta_{SHE}[j_s \times \frac{M}{\mid M \mid}], \tag{4.10}$$

$$j_s \propto \Delta\alpha(M \times \frac{dM}{dt}), \tag{4.11}$$

$$R(t) = R_0 \cos(\omega t + \Phi), \tag{4.12}$$

where θ_{SHE} is the spin hall angle. Spin is related to charge current efficiency.

Therefore, V_{ISHE} can be calculated based on Figure 4.3.[34]

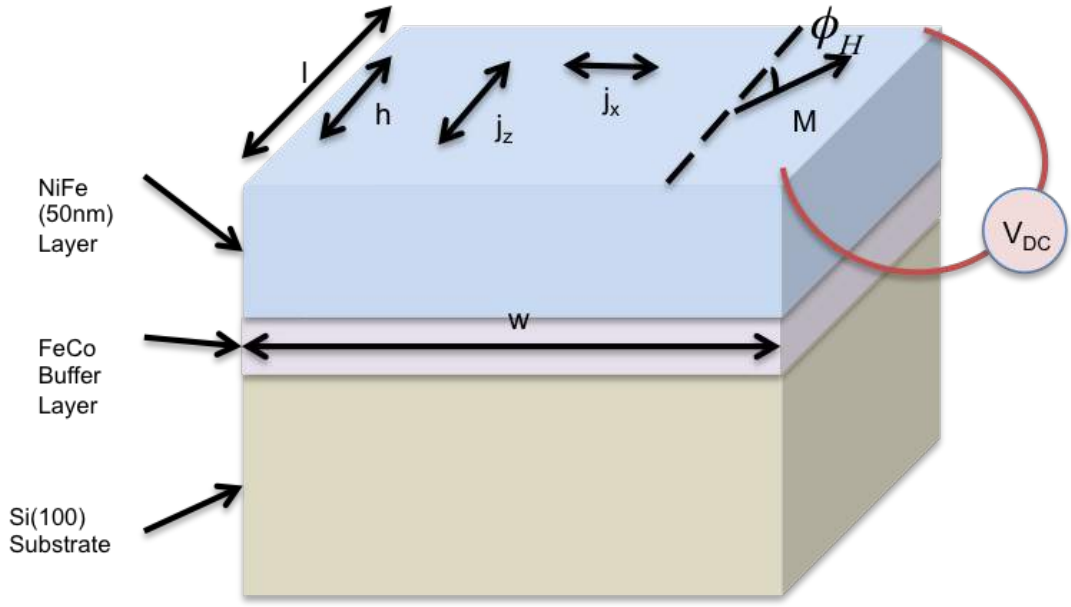

FIGURE 4.3: Vectors in an NiFe(50nm)/FeCo($t$nm) sample. Figure not drawn to scale.

Since

$$V_{DC} = A_L L + A_D D, \tag{4.13}$$

where

$$A_L = -V_{AMR} \sin\Phi \sin(\phi_H) \cos 2\phi_H - V_{AHE} \cos\Phi \sin\phi_H + ISHE \sin^3\phi_H, \tag{4.14}$$

and

$$A_D = V_{AMR} \cos\Phi \sin\phi_H \cos 2\phi_H - V_{AHE} \sin\Phi \sin\phi_H, \tag{4.15}$$

by simultaneously manually fitting the angular dependences of A_L and A_D,[34] the presence of spin pumping can be determined by a non-zero value of V_{ISHE}. However, the values of V_{ISHE} here do not allow for much comparison among samples due to the different amounts of total voltage passed through each sample. Therefore, from this method, it is difficult to determine which thin film sample has more spin pumping than another.

To compare the amounts of spin pumping among different thin film samples, Spin Hall Effect (SHE) needs to be considered. SHE has intrinsic and extrinsic origins. Its intrinsic origin is the effective gauge field which is due to spin-dependent, intrinsic spin-orbit interaction. Its extrinsic origin involves side jump and skew scattering mechanisms, which are mediated by spin-orbit interactions with magnetic impurities.[37]

V_{ISHE} can be calculated from[37]

$$V_{ISHE} = \frac{l}{\sigma_{NiFe} t_{NiFe} + \sigma_{MnIr} t} \{\theta_{SHE} \lambda_d (\frac{2e}{\hbar}) \tanh(\frac{t}{2\lambda_d}) j_s\}, \tag{4.16}$$

where $g_{\uparrow\downarrow} = 2\sqrt{3}\pi M_s t_{NiFe}(\alpha_{NiFe/MnIr} - \alpha_{NiFe})/\mu_B$ is the spin mixing conductance, σ and t are the respective conductivities and thicknesses of the corresponding layers, $\hbar$ is Planck's constant, e is electron charge and μ_B is the Bohr magneton and

$$j_s = \frac{g_{\uparrow\downarrow} \gamma^2 h^2 \hbar l [4\pi M_s \gamma + \sqrt{(4\pi M_s \gamma)^2 + 4\omega^2}]}{8\pi \alpha^2_{NiFe/MnIr} [(4\pi M_s \gamma)^2 + 4\omega^2]} \tag{4.17}$$

4.2.4 Using Electrical Method to Measure Spin Hall Angle

By doing a fitting of microwave power P against t, spin hall angles θ_{SHE} and diffusion length λ_d of MnIr can then be calculated using equation 4.18[37]

$$\begin{aligned} P &= V_{ISHE}(\frac{\hbar}{2e}) \frac{8\pi \alpha^2_{NiFe/MnIr} (\sigma_{NiFe} t_{NiFe} + \sigma_{MnIr} t)[(4\pi M_s \gamma)^2 + 4\omega^2]}{g_{\uparrow\downarrow} \gamma^2 h^2 \hbar l [4\pi M_s \gamma + \sqrt{(4\pi M_s \gamma)^2 + 4\omega^2}]} \\ &= \theta_{SHE} \lambda_d \tanh(\frac{t}{2\lambda_d}). \end{aligned} \tag{4.18}$$

High θ_{SHE} imply that the particular material can be used as an efficient source of spin currents, so as to manipulate magnetization.[37]

Therefore, equation 4.18 is used to estimate the values of θ_{SHE} and λ_d so that the amount of spin pumping in each sample can be calculated using equation 4.16.

Chapter 5

Results and Discussion

This chapter focuses on the results obtained after analysis was conducted on experimental data, as well as discusses the results obtained. In this chapter, the different magnetization relaxation processes in the two types of thin films were identified and I attempted quantifying them. Although spin pumping is an extrinsic damping process, I shall not include it when referring to extrinsic contributions to damping in this chapter, since it was accounted for in α.

5.1 NiFe Film with Buffer Layer of FeCo

5.1.1 Ruling out Extrinsic Contribution to Linewidth

Considering the data from VNA, when the data was fitted using equation 4.3, the parameters obtained were ΔH_0, which is made up of the inhomogeneous line broadening ΔH_{mosaic} and the two-magnon scattering contribution ΔH_{TMS}, and Gilbert damping constant α.

The frequency sweep is carried out in one of the directions of the easy axis, at $\phi_H =$ 90 degrees. Looking at frequency-dependent SRE data, the same parameters were gotten when the FMR linewidth ΔH was plotted against frequency for the 4 thin film samples according to equation 4.3. From the apparent linearity of the graphs, as shown in Figure 5.1, and seeing how the graphs fit so well with equation 4.3, it suggests that the contribution to the FMR linewidth is mainly intrinsic. This is supported by the coefficients of determination of the 4 graphs, which are all above

0.962, suggesting that the magnetic dissipation was mainly intrinsic and that there was negligible extrinsic damping, and thus, negligible two-magnon scattering.

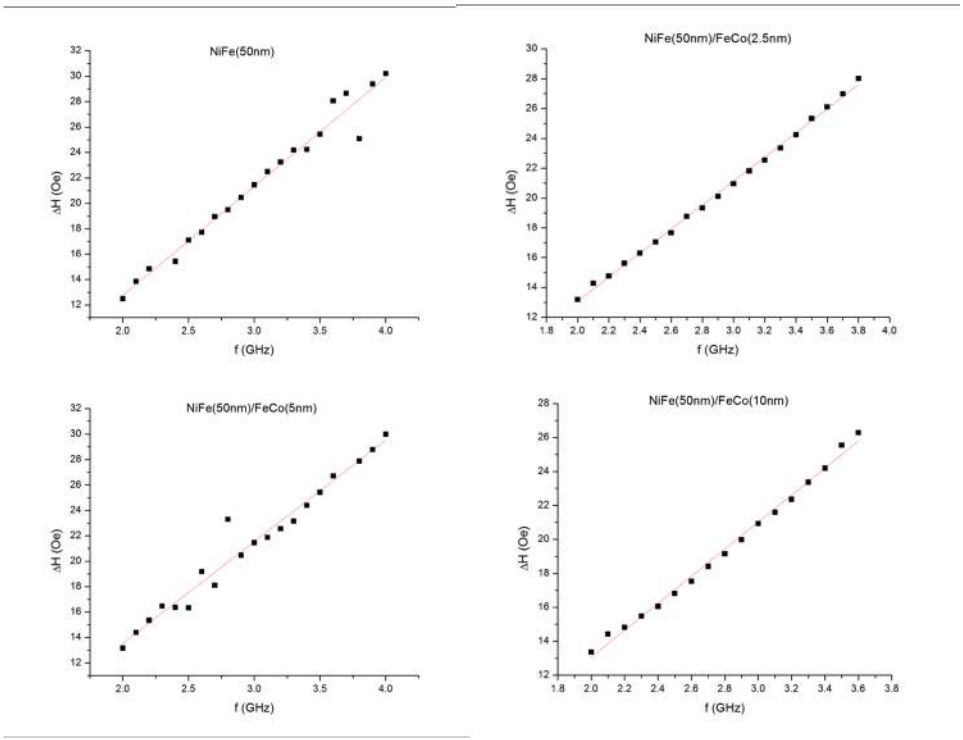

FIGURE 5.1: Graphs of NiFe(50nm)/FeCo($t$nm) samples when data was fitted to equation 4.3

	VNA				**SRE**			
Thickness of FeCo layer (nm)	0	2.5	5	10	0	2.5	5	10
ΔH_0	-0.348	0.0727	0.108	0.399	-4.399	-3.054	-2.463	-2.870
Gilbert Damping Constant α	0.01091	0.01018	0.01007	0.01047	0.01201	0.01129	0.01120	0.01115

TABLE 5.1: Parameters of NiFe(50nm)/FeCo($t$nm) samples when data was fitted to equation 4.3

The values for ΔH_0 are stated in Table 5.1. From the low values of ΔH_0 that we obtain of the samples from the transmission line method via VNA, this supports the above conclusion that two-magnon scattering is a negligible source of magnetization relaxation process in the magnetic thin films. However, the ΔH_0 values obtained from the electrical detection method via SRE are relatively high. Therefore, this method is not the most accurate in determining the presence of two-magnon scattering.

Any deviations from the best fit curves could be due to inhomogeneities in the samples. However, as the data points are almost all approximately close to the best fit curves, this shows that the samples are largely homogeneous. In addition,

the discrepancies that we see in the values of the parameters attained using the two different methods, could be due to the difference in the strengths of magnetic fields applied. However, the trends for the different parameters for the two methods are roughly the same.

A more accurate method to determine the existence or non-existence of extrinsic contribution would be to fit the angular-dependent SRE data with equation 4.9. When this was conducted, there results further suggests that there is negligible two-magnon scattering contribution. Although the fitting in Figure 5.2 is not good, the best fit does give approximately a straight line, which would suggest that contribution from two-magnon scattering is negligible. Unfortunately, it was impossible to exactly quantify the extrinsic contribution in the samples due to the large number of parameters that needed to be fitted, as well as the randomness of the defects in the samples, instead of them being rectangular-shaped.

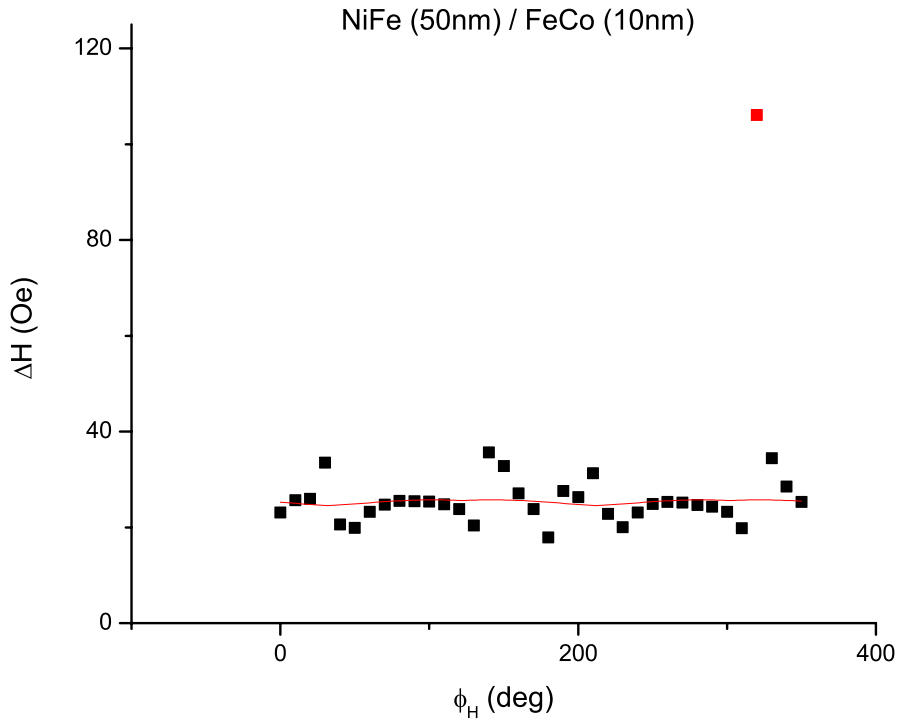

FIGURE 5.2: Graph attained from NiFe(50nm)/FeCo(10nm) samples when data was fitted to equation 4.9

5.1.2 Spin Pumping

Analyzing data from VNA and frequency-dependent SRE measurements, the Gilbert damping constants α were attained for all 4 thin film samples and can be seen in Table 5.1. While each thin film sample has two different values due to the two methods employed to get the values, the trend is evident for both methods. The Gilbert damping constant is highest for the single layer of NiFe thin film sample. However, when the FeCo buffer layer is added to the thin film sample, the Gilbert damping constant drops. The Gilbert damping constant then stays relatively constant for the different thicknesses of the FeCo buffer layer.

As can be seen from Figure 5.3, there is a small increase in α for the SRE method from an FeCo thickness of 5 nm to 10 nm. This is at odds with the trend observed for the VNA method, which continues its decreasing trend. However, it is likely that this small increase is possible as well. Permalloy is known to have low α due to its low anisotropy in comparing with FeCo. Therefore, it is possible that α were to increase slightly as FeCo thickness increases. However, we are unable to determine with certainty if this increase does occur as FeCo thickness increases due to the difference in data. What we can determine is that the α values is highest for the single layer of NiFe thin film sample before decreasing and stabilizing with increasing thickness of the FeCo layer.

A possible reason for the drop in Gilbert damping constant could be due to the spin pumping damping process. Spin current pumped from either NiFe layer to FeCo buffer layer or vice versa is converted to a charge current due to ISHE, which can be measured as a DC voltage.[35] Since both layers are ferromagnetic materials, net spin current in either direction is possible. From fitting the data for the NiFe(50nm)/FeCo(5nm) and NiFe(50nm)/FeCo(10nm) thin film samples with equations 4.14 and 4.15, it was found that there was Inverse Spin Hall Effect (ISHE). This means that there was net spin pumping from the NiFe layer to the FeCo buffer layer or vice versa. The values of the different parameters of equations 4.14 and 4.15 for the thin film samples with buffer layers of 5 nm and 10 nm are listed in Table 5.2.

The fittings of equations 4.14 and 4.15 with the data from the NiFe(50nm)/FeCo(10nm) thin film sample can be seen in Figure 5.4. As the fittings are close to the data points, the parameters obtained are highly accurate.

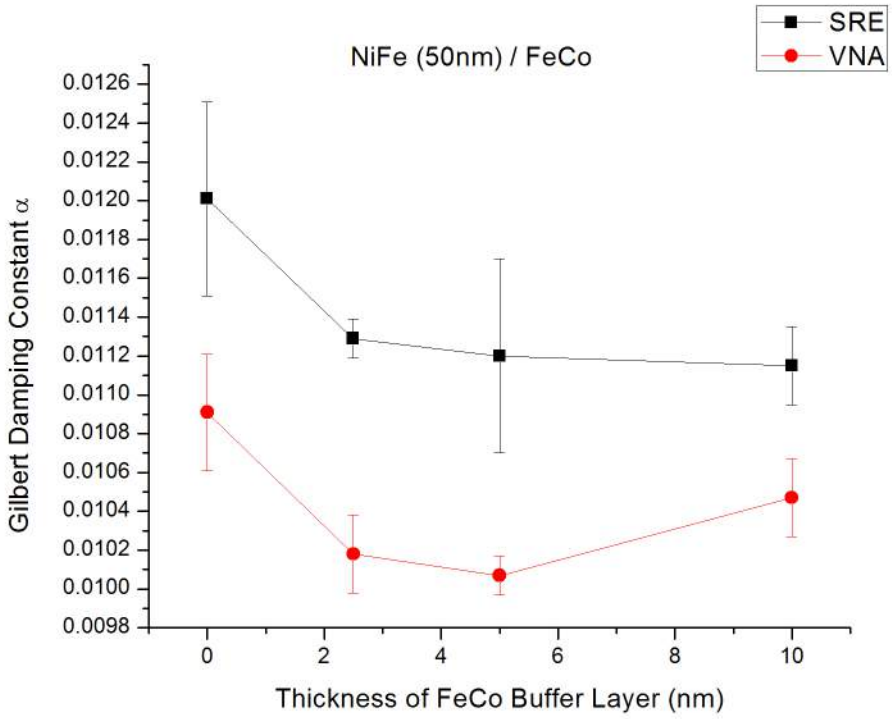

FIGURE 5.3: Gilbert damping constant α values of NiFe(50nm)/FeCo($t$nm)

	NiFe (50nm) / FeCo (5nm)	**NiFe (50nm) / FeCo (10nm)**
ISHE (μV)	0.025	0.15
AMR$_x$ (μV)	0.82	0.9
AHE (μV)	0.055	0.09

TABLE 5.2: Determining the parameters for NiFe(50nm)/FeCo(5nm) and NiFe(50nm)/FeCo(10nm) samples when data was manually fitted to equations 4.14 and 4.15

5.2 NiFe/MnIr Exchange-Biased Thin Film

This entire experiment was carried out twice. All results stated here are from the first batch of thin film samples, unless otherwise stated. While the trend was relatively the same for both sets of thin film samples, there are also some differences. The differences can be attributed to different sputtering conditions or some thin film samples being defective. However, these differences do not affect the overall trends or results of my project. Since the trends obtained for the α values of the NiFe/FeCo thin film samples were relatively the same for the VNA and SRE methods, I only used the SRE method for the measurements of the NiFe/MnIr thin film samples.

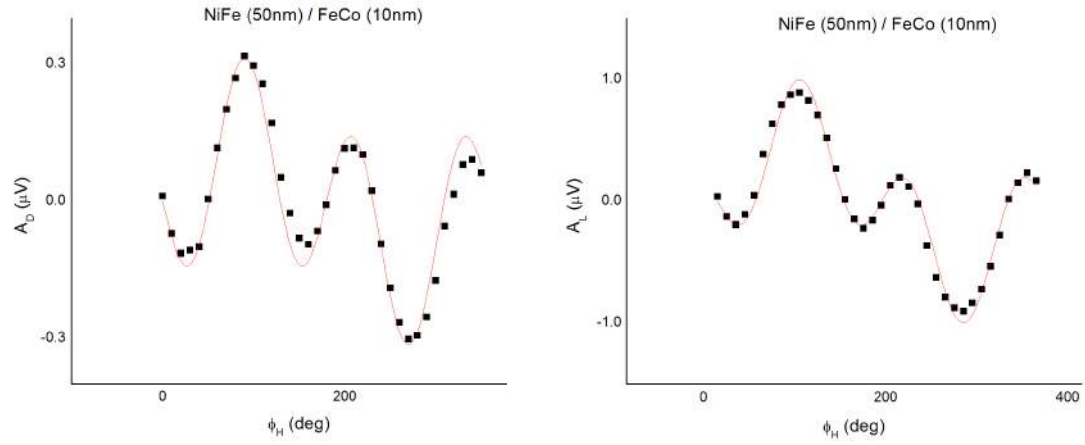

(A) Data fitted to equation 4.15 (B) Data fitted to equation 4.14

FIGURE 5.4: Plots of NiFe(50nm)/FeCo(10nm) sample when data was manually fitted to equations 4.15 and 4.14 to determine the presence of ISHE

5.2.1 Structure of NiFe(50nm)/MnIr(*x*nm)

MnIr is an antiferromagnetic, face-centered cubic (fcc) crystal with Mn atoms on 3 out of 4 cubic sublattices. The Mn sublattice can be seen as made up of 2-dimensional kagome lattices stacked along the (111) direction. The Mn moments have strong 3-sublattice triangular (T1) magnetic order and a high magnetic transition temperature due to inter-kagome coupling and strong magnetic anisotropy. This leads to a non-zero net intrinsic AHE. The structure of MnIr can be seen in Figure 5.5.[36]

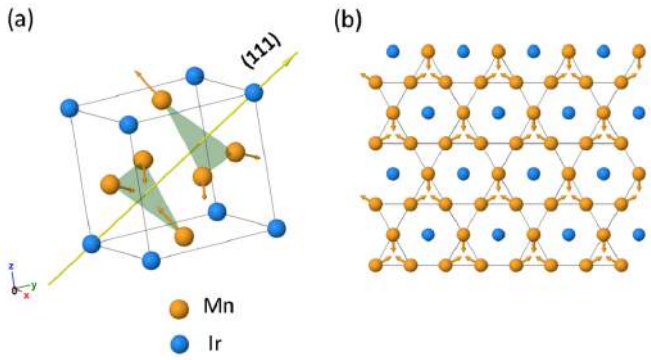

FIGURE 5.5: Structure of MnIr[36]

MnIr has been found to exhibit large Spin Hall Effect (SHE).[36] For my project, I will characterize SHE detection of MnIr in relation to exchange bias since both

are highly dependent on interface.

5.2.2 Typical V_{DC} Spectra

When the data of the thin film samples from angular-dependent SRE measurements were fitted to equation 4.5, an example the graphs obtained is as shown in Figure 5.6, where the NiFe(50nm)/MnIr(12nm) sample at ϕ_H=90 degrees was used as an example. This spectra is typical of a V_{DC} spectra and the other spectras are similar to the spectra displayed in Figure 5.6.

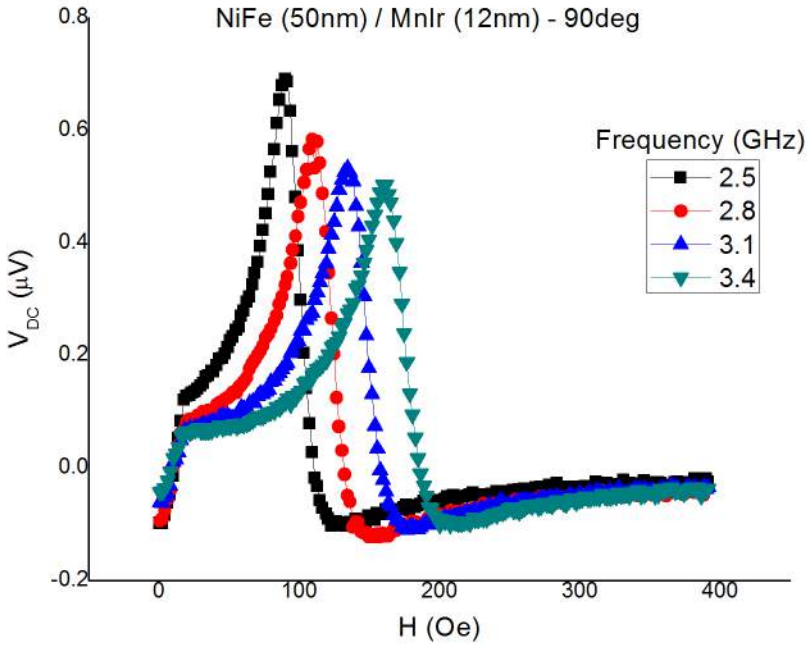

FIGURE 5.6: Graph of NiFe(50nm)/MnIr(12nm) sample at ϕ_H=90 degrees

The unusually steep slope that is seen in Figure 5.6 from 0 Oe to 20 Oe is a hysteretic feature, which come about from static magnetization. During that magnetic field range, the spins in the FM layer flip abruptly for all the different frequencies measured due to the fact that exchange bias is independent of frequency.

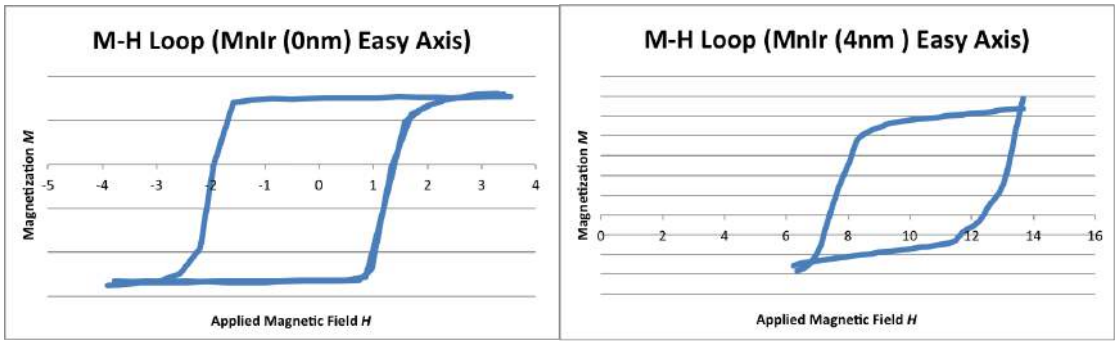

(A) NiFe(50nm) sample (B) NiFe(50nm)/MnIr(4nm) sample

FIGURE 5.7: M-H loops of thin film samples

5.2.3 Evidence of Exchange Bias

From the M-H loops of the easy axes of the first batch of different thin film samples obtained from the MH loop tracer, it can be confirmed as expected that the M-H loops are shifted after a certain thickness of the MnIr layer. The hysteresis loops for the single layer NiFe(50nm) sample and NiFe(50nm)/MnIr(4nm) sample are shown in Figure 5.7 to demonstrate the horizontal shift in the M-H loops. Any vertical shift in the hysteresis loops are disregarded as the MH loop tracer had not been calibrated for the vertical axis.

In addition, the coercivity values also increase when the MnIr layer has a thickness of 2nm. These coercivity values, obtained from the M-H loop tracer, are also listed in Table 5.3.

Thickness of MnIr layer (nm)	0	1	2	4	6	8	12
Coercivity H_c (Oe)	1.769	2.440	12.017	2.745	3.965	1.586	2.623

TABLE 5.3: Coercivity H_c of NiFe(50nm)/MnIr($t$nm) thin film samples

After fitting the data of the different samples from angular-dependent SRE measurements with equation 4.6, the values of exchange bias field H_e, anisotropy field H_a and rotational anisotropy field H_{ra} were obtained for each sample and can be seen graphically in Figure 5.8.

From Figure 5.8, it is evident that when the AF layer thickness $t_{AF} < 2$ nm, the exchange bias field H_e is almost zero. The rotatable anisotropy field H_{ra} increases sharply from t_{AF}=1 nm to t_{AF}=2 nm. The increase in H_{ra} is due to the establishment of AF order of the MnIr layer. However, we can determine that AF order is still in the rotatable AF grain regime and are thus, unstable, as H_e

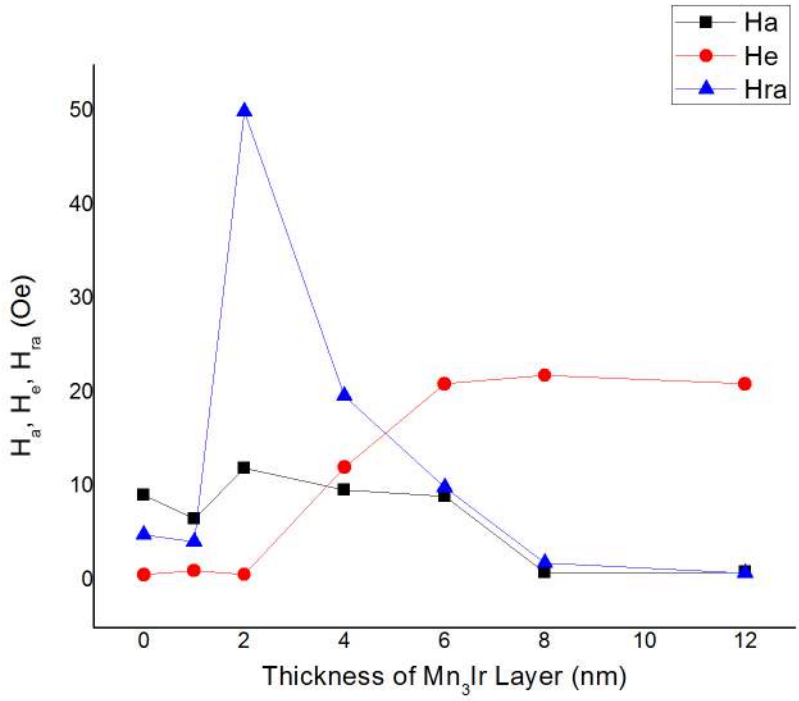

FIGURE 5.8: Exchange bias field H_e, anisotropy field H_a and rotational anisotropy field H_{ra} of NiFe(50nm)/MnIr($x$nm) samples

is almost zero. It was also observed that H_{ra} is maximum at t_{AF} =2nm before decreasing at $t_{AF} > 2$ nm. On the other hand, H_e increases and saturates once $t_{AF} > 2$ nm. The opposing trends of H_e and H_{ra} at $t_{AF} > 2$ nm can be attributed to an increasing number of rotatable AF grains becoming stable. This suggests that the critical thickness of the MnIr layer is 2 nm and that exchange bias only sets in when $t_{AF} > 2$ nm.

These trends are supported by the second batch of thin film samples.

Since it has been found that there is exchange bias in thin film samples with $t_{AF} > 2$ nm, there is possibly exchange coupling in these samples. Exchange coupling is an extrinsic magnetization relaxation process. When the AF spins are pinned to the FM spins at the interface, the AF spins drag the FM precession, causing damping in the sample.

It was also decided to attempt to sputter without an external magnetic field to obtain samples without exchange bias so as to determine the effects of exchange bias on the thin film samples. However, I was unable to achieve this because there

was still a stray field in the sputtering chamber, resulting in exchange bias in the samples.

5.2.4 Extrinsic Contribution to Damping

The frequency sweeps are carried out in both directions of the easy axis, at ϕ_H=90 degrees and ϕ_H=270 degrees. From the frequency-dependent SRE data, when ΔH was plotted against frequency for the 7 thin film samples according to equation 4.3, it is possible that there is extrinsic contribution to damping, unlike the previous type of thin film. The graphs attained from equation 4.3 for the NiFe(50nm)/MnIr(1nm) and NiFe(50nm)/MnIr(12nm) samples are displayed in Figure 5.9. Compared to Figure 5.1, the graphs do not fit as well with equation 4.3. It can be seen that the graph from the frequency sweep of the NiFe(50nm)/MnIr(12nm) when ϕ_H=270 degree direction is slightly curvy, which is consistent with two-magnon scattering.

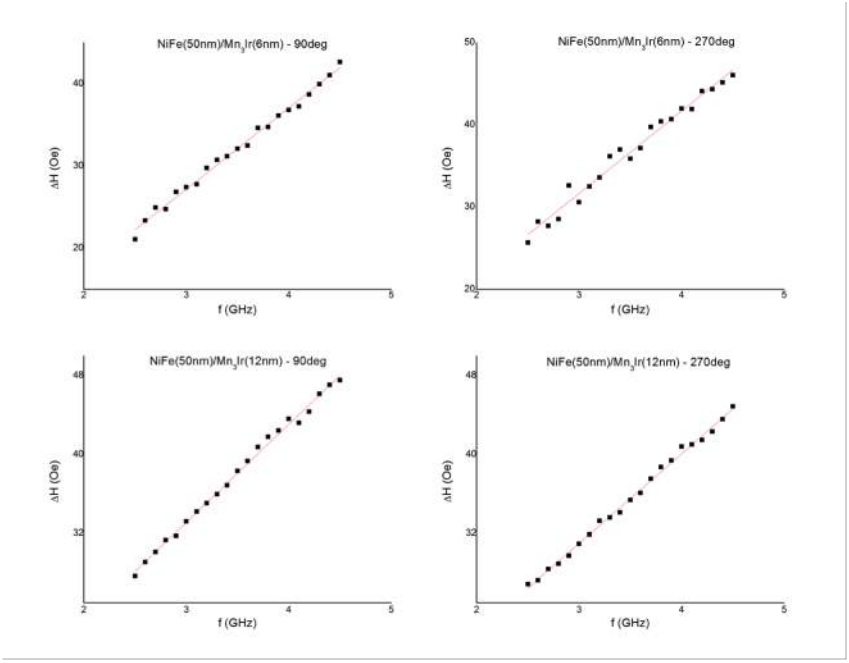

FIGURE 5.9: Graphs of NiFe(50nm)/MnIr($t$nm) samples when data was fitted to equation 4.3

The values for ΔH_0 are stated in Table 5.4. From the quite high values of ΔH_0 that can be seen for the thin film samples MnIr layers of 1 nm, 2 nm, 6 nm, 8 nm and 12 nm, this supports the above theory of extrinsic damping. In addition, the α and ΔH_0 values in both directions are inconsistent for their respective samples,

further suggesting that there could be extrinsic magnetization relaxation processes present in at least a few of the samples. However, an anomaly to be noted is that there is a huge difference in α values for the single layer NiFe sample, which should not be the case since there is no MnIr layer in contact with NiFe. In addition, the parameters obtained when the data for these samples were fitted with equation 4.3 are not accurate as equation 4.3 is assumed to be linear. Therefore, equation 4.3 is no longer a good fit when there are extrinsic damping magnetization processes, such as two-magnon scattering and exchange coupling, in the sample. However, I was unable to determine the exact contributions of two-magnon scattering and exchange coupling.

Thickness of MnIr layer (nm)	0	1	2	4	6	8	12
α **at** ϕ_H**=90 degrees**	0.0111	0.0130	0.0135	0.0158	0.0148	0.0152	0.0139
ΔH_0 **at** ϕ_H**=90 degrees**	-0.0364	2.28	2.79	-0.619	-0.385	-4.59	3.33
α **at** ϕ_H**=270 degrees**	0.0137	0.0124	0.0152	0.0160	0.0140	0.0151	0.0127
ΔH_0 **at** ϕ_H**=270 degree**s	-4.02	1.91	0.390	-0.925	1.63	-2.90	3.78

TABLE 5.4: Values of α and ΔH_0 of NiFe(50nm)/MnIr($t$nm) samples when ϕ_H=90 and ϕ_H=270 degrees

The best method to determine if there is extrinsic contribution to damping is to fit the data from angular-dependent SRE method with equation 4.9. The damping is largely intrinsic, with negligible extrinsic damping, if the fitting is approximately a straight line. Once again, it was impossible to exactly quantify the extrinsic contribution in the samples due to the large number of parameters that needed to be fitted, as well as the randomness of the defects in the samples, instead of them being rectangular-shaped.

From fitting the angular-dependent SRE data with equation 4.9, it can be determined that while it appears to be that the single layer NiFe sample has negligible extrinsic damping since the fitting is approximately a straight line, similar to what was seen in Figure 5.1, this is not the case for the other samples. This can be seen in Figure 5.10, which is of the NiFe(50nm)/MnIr(2nm) sample. The best fit attained for that sample is not a straight line but a curved one, thus suggesting that there are two-magnon scattering and exchange coupling contributions. This is the same for other samples with $t_{AF}\geq$1nm. Therefore, there is non-negligible extrinsic damping for samples with $t_{AF}\geq$1nm.

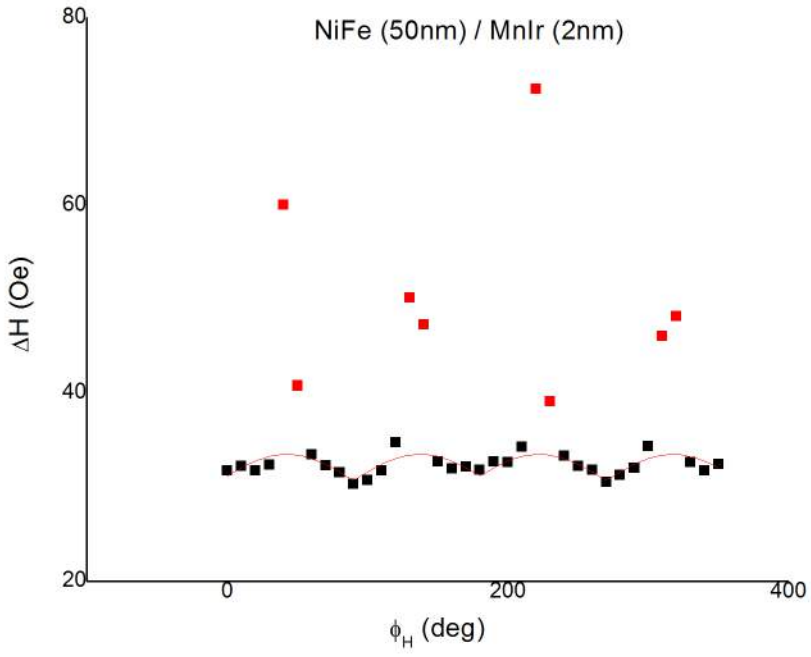

FIGURE 5.10: Graphs of NiFe(50nm)/MnIr(10nm) samples when data was fitted to equation 4.9

5.2.5 Spin Pumping

The Gilbert damping constants α are inaccurate as we can see from the subsection 5.2.4, since ΔH_0 was assumed to be frequency-independent due to the negligence of two-magnon scattering. However, since there is non-negligible two-magnon scattering, ΔH_0 is thus frequency-dependent. Therefore, the best way would be to use angular-dependent SRE data since frequency was kept constant for that experiment. Due to non-negligible two-magnon scattering contribution, the α values are different in both the $\phi_H = 90$ degree and $\phi_H = 270$ degree directions. Since the α values are still of importance, the effective α values are listed in Table 5.5 and displayed in Figure 5.11. However, it should be noted that caution should be taken when using these values.

Thickness of MnIr layer (nm)	0	1	2	4	6	8	12
Gilbert Damping Constant α	0.0124	0.0127	0.0144	0.0159	0.0144	0.0152	0.0133

TABLE 5.5: Values of α for NiFe(50nm)/MnIr($t$nm) samples

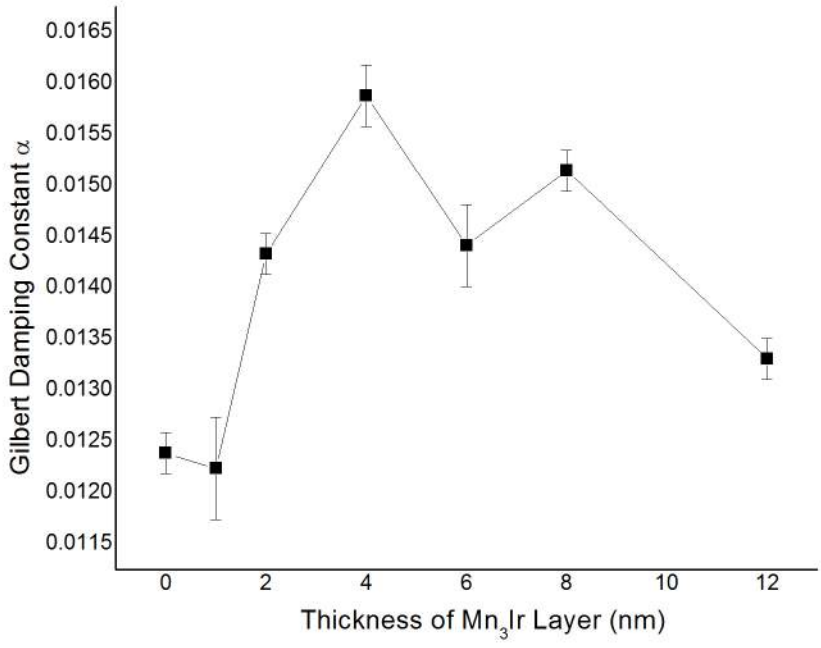

FIGURE 5.11: Graphical representation of α for NiFe(50nm)/MnIr($t$nm) samples

From Table 5.5 and Figure 5.11, we can see that the values of α are low and relatively constant when $t_{AF} \leq 1$ nm. From $t_{AF} = 1$ nm to $t_{AF} = 2$ nm, the value of α increases. There does not appear to be a trend when $t_{AF} \geq 2$ nm, except that the α values when $t_{AF} \geq 2$ nm are larger than the single layer of NiFe. This could be due to the inaccurate values of α since there are extrinsic magnetization relaxation processes in the films where $t_{AF} \geq 2$ nm. However, these values can still be used to look out for trends.

A possible reason for the increase in Gilbert damping constant α could be due to spin pumping. Spin current moves from the FM NiFe material to the AF MnIr material, transporting angular spin momentum into the MnIr material. This causes the spins in the NiFe layer to lose angular momentum. Therefore, damping increases in a sample when a MnIr layer is placed on a NiFe layer, which is in line with what we see from Table 5.5, regarding the increase in α values as $t_{AF} \geq 2$ nm.

The angular-dependent SRE data for the thin film samples were manually fitted with equations 4.14 and 4.15. An example of the graphs obtained when these

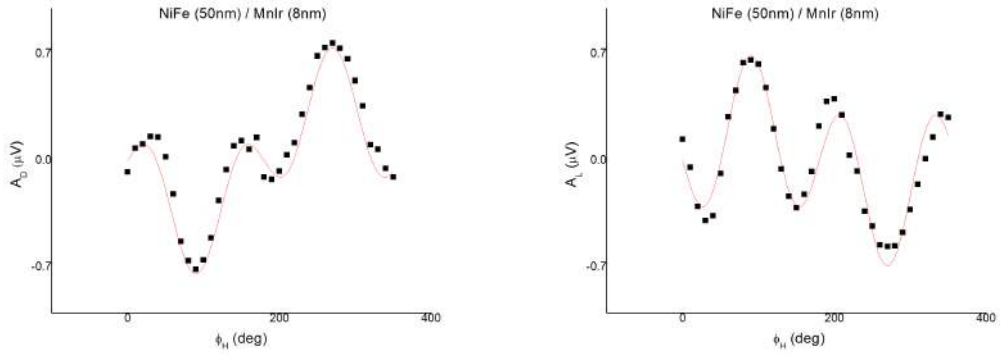

(A) Data fitted to equation 4.15 (B) Data fitted to equation 4.14

FIGURE 5.12: Data manually fitted to determine the presence of ISHE

fittings were done are displayed in Figure 5.12 for the t_{AF}=8nm sample. The other samples also displayed similar fittings after the data had been manually fitted.

From the fittings of the data, it was found that there was Inverse Spin Hall Effect (ISHE) for $t_{AF} \geq 1$ nm since the values for V_{ISHE} for these samples were non-zero. This means that there was spin pumping from the NiFe layer to the MnIr layer. The values of the different parameters of equations 4.14 and 4.15 for the thin film samples are listed in Table 5.6 and shown in Figure 5.13.

Thickness of MnIr layer (nm)	0	1	2	4	6	8	12
$\mathbf{V}_{ISHE}$ **(μV)**	0	0.18	0.057	0.16	0.1	0.14	0.093
$\mathbf{V}_{AMR_x}$ **(μV)**	1.2	0.91	0.86	1.15	0.85	1.1	0.7
$\mathbf{V}_{AHE}$ **(μV)**	0.24	0.15	0.26	0.2	0.13	0.17	0.1
Microwave Phase Φ (degrees)	60	60	60	61	62	57	60

TABLE 5.6: Determining the parameters for NiFe(50nm)/MnIr($t$nm) samples when data was manually fitted to equations 4.14 and 4.15

From Table 5.6 and Figure 5.13, we can see that the contribution from AMR to total voltage is much larger than the contributions from AHE or ISHE, which are about the same. In addition, from Table 5.6, the microwave phase Φ is about 60 degrees for all 7 samples. The microwave phase Φ is similar for all the samples as the samples are made of the same materials and thus, the microwave propagation properties are similar.

Now, I shall attempt to quantify the amount of spin pumping in each sample by using equation 4.16. However, to be sure that the increase in Gilbert damping

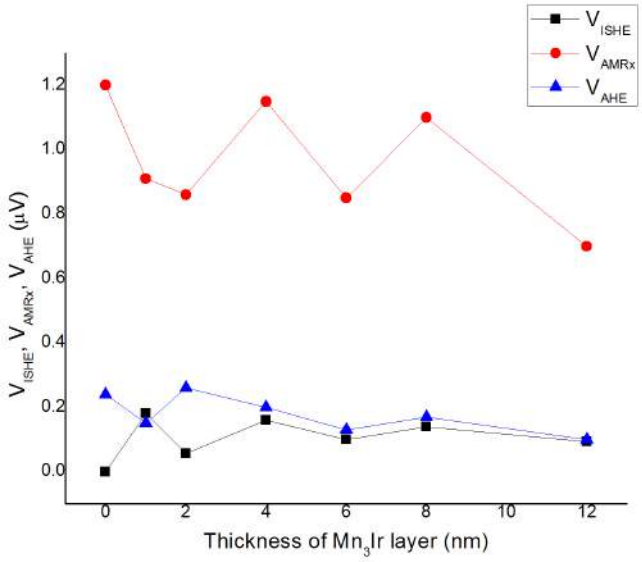

FIGURE 5.13: Graphical representation of the parameters for NiFe(50nm)/MnIr($t$nm) samples when data was manually fitted to equations 4.14 and 4.15

constant alpha is purely due to spin pumping, ΔH_0 has to be fitted to be small so that we can neglect the two-magnon scattering contribution. This was not the case as we found out from subsection 5.2.4, where it was found that there was non-negligible two-magnon scattering from samples where $t_{AF} \geq 1$ nm. In addition, since Gilbert damping constant alpha is not very accurate due to the contribution to damping due to extrinsic contribution, this method to quantify spin pumping is unusable. Therefore, it is also not possible to calculate θ_{SHE} and diffusion length λ_d using equation 4.18 when a fitting was conducted of microwave power P against thickness of MnIr t. It was expected that theoretically, a high value of θ_{SHE} would be obtained due to the T1 MnIr structure.[37] Therefore, the amount of spin pumping in each sample also cannot be calculated using equation 4.16 as θ_{SHE} and λ_d cannot be estimated.

Another possible method to analyze spin pumping in this type of magnetic thin film is by considering the percentage of the total voltage of each sample that is contributed by V_{ISHE}. This can be seen in Table 5.7.

It would be expected, that the higher the percentage of V_{ISHE} compared to total voltage, the higher the contribution of spin pumping and thus, the higher the Gilbert damping constant α. Ignoring the $t_{AF} = 1$ nm and $t_{AF} = 12$ nm samples,

Thickness of MnIr layer (nm)	0	1	2	4	6	8	12
Gilbert damping constant α	0.0124	0.0127	0.0144	0.0159	0.0144	0.0152	0.0133
Percentage of V_{ISHE} **(%)**	0	14.5	4.84	10.6	9.26	9.93	10.4

TABLE 5.7: Percentage of V_{ISHE} in comparison with total voltage for NiFe(50nm)/MnIr($t$nm) samples

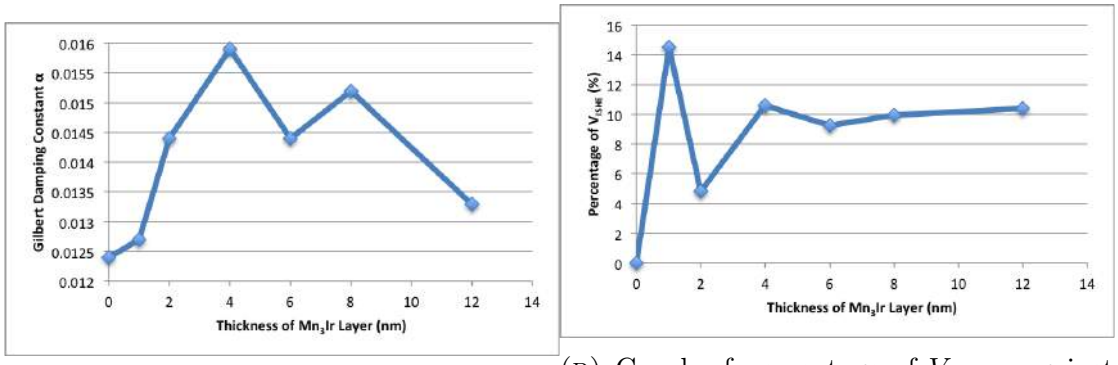

(A) Graph of α against t_{MnIr}

(B) Graph of percentage of V_{ISHE} against t_{MnIr}

FIGURE 5.14: Plots of α and percentage of V_{ISHE} against thickness of MnIr layers

it is evident that the trends for Figures 5.14a and 5.14b are about the same. For example, when there was an increase in α for the samples $t_{AF} = 2$ nm to $t_{AF} = 4$ nm, there was also an increase in percentage of V_{ISHE} for the samples $t_{AF} = 2$ nm to $t_{AF} = 4$nm. Therefore, an increase or decrease in α corresponds with there being a larger or smaller contribution from spin pumping for most samples.. However, this method is also not very accurate as the values of α are also quite inaccurate in the first place, which could be why the $t_{AF} = 1$ nm and $t_{AF} = 12$ nm samples did not follow the trend.

5.3 Reasons for Elimination of Other Magnetic Relaxation Processes

There are many relaxation processes that can be ruled out to exist in the thin film samples.

Charge transfer relaxation is only present in ferrites.[10] Since neither permalloy, FeCo or MnIr is a ferrite, this process does not exist in the thin film samples.

For the next two processes, they only exist if there are rare-earth elements, such as scandium and yttrium, in the thin film samples.[10] Since there are no rare-earth

elements present in the materials used to make up the thin film samples, **slowly relaxing impurity** and **rapidly relaxing impurity** are no possibility of being present in the samples.

Damping due to **eddy current** decreases exponentially in a range of 1 micron, which is the skin depth. Since the samples are in the range of 50 to 70 nm, the difference in damping due to eddy current between the samples is negligible, thus resulting in negligible contribution to Gilbert damping constant for all thin film samples.[10]

Three-magnon scattering and **four-magnon scattering** do not take contribute to damping in the thin film samples due to the field/film configuration. The occurrence of these scattering processes depends on the availability of degenerate spin-wave modes. The number of the degenerate modes by conducting FMR measurements with a static magnetic field perpendicular to the film plane.[10] Therefore, these two processes can be rules out.

However, there are a few damping processes that are actually present in the thin film samples for both types of thin films, However, only the magnetization relaxation processes mentioned earlier in Chapter 5 are responsible for the differences in intrinsic and extrinsic damping between the different samples.

Spin-flip magnon-electron scattering and **breathing Fermi surface** are processes that are present in materials with free electrons.[10] Since there are free electrons in the permalloy and FeCo layers, these magnetization relaxation processes exist in all the thin film samples fabricated throughout my project. These two processes are dependent on temperature. As temperature increases, the electron lifetime decreases. This causes the electron Fermi level to broaden, resulting in the magnon-electron scattering probability increasing and thus, damping increasing due to spin-flip magnon-electron scattering.

An increase in electron lifetime, on the other hand, due to the increase in temperature causes the system to move further away from equilibrium. Therefore, more energy dissipation to the lattice due to breathing fermi surface and thus, damping increases. However, since temperature is maintained throughout all the experiments, these two magnetization relaxation processes will be constant in all the samples fabricated and are not responsible for any differences in damping among the samples.

Magnon-phonon scattering is a process that takes place in practically all magnetic materials. However, since temperature and the range of magnetic field applied to the different thin film samples are the same, the difference in damping between the different samples is not due to magnon-phonon scattering and can be neglected.[10]

Chapter 6

Future Work

There are many possible ways to follow up with the results from my project.

One idea to insert a copper spacer in between the NiFe and MnIr layers. By doing so, there shall not be any exchange bias effect and thus, negligible extrinsic contribution, as the NiFe and MnIr layers are no longer in contact. Therefore, it is possible to focus purely on the spin pumping contribution to the samples. The values of α will be more accurate and it will be possible to use equation 4.18 to calculate θ_{SHE} and λ_d of that particular type of thin film.

Another way could be to determine the effects of exchange bias and magnetization relaxation processes when temperature is varied by attaching a heater during VNA measurement. It has been found that many parameters such as saturation magnetization M_s, dynamic magnetic anisotropy field H_k^{dyn} and Gilbert damping constant α could change with the effect of temperature.[5] It would be interesting if this applied to this type of thin film too and how the damping processes would vary when temperature was varied.

It would also be interesting to consider how damping changes when there is an oblique angle. An oblique angle occurs when substrates are at different angles during the sputter deposition process. Magnetic thin film samples fabricated with oblique angles have strong uniaxial anisotropy and tilted columnar grain structures are grown with respect to substrate. There are two main effects, shape anisotropy

and magnetocrystalline anisotropy, which both contribute to the observed magnetic anisotropy of the films.[13] Therefore, it is probable that magnetization relaxation processes vary when thin film samples are grown at an oblique angle for these materials.

Since some of the layers in the thin film samples are quite thin like $t_{AF} = 1$ nm, better results might be obtained if the power sputtering was lowered and thus, a longer deposition time was given to sputter the material onto the substrate, so that the thicknesses of each material are closer to the desired thicknesses.

Chapter 7

Conclusion

In this report, different types of magnetic thin films were fabricated using radio-frequency sputtering and studied using the VNA, Magnetic Hysteresis Loop Tracer and SRE method. The two types of thin films that were fabricated was a NiFe film with a buffer layer of FeCo, as well as an exchanged-biased ferromagnetic/antiferromagnetic NiFe/MnIr film. The thickness of the FeCo buffer layer and the antiferromagnetic MnIr layer was varied to produce multiple thin film samples. Numerical analyses was then used to identify and attempt to quantify the different magnetization relaxation processes present in the different samples.

It was found that for the NiFe film with a buffer layer of FeCo, the only magnetization relaxation process that differentiated in amount among the samples was spin pumping, which caused the Gilbert damping constant α to vary from the single layer NiFe α value. There was found to be no extrinsic damping after the data was fitted with equations adapted from various papers.

As for the ferromagnetic/antiferromagnetic NiFe/MnIr film, there was found to be exchange bias after the critical thickness of 2 nm for the MnIr layer, was passed. The values of α also increased once this critical thickness was reached and stayed constantly higher than the single layer NiFe α value. This increase was attributed to spin pumping from the NiFe layer to the MnIr layer. However, it was found that the values of α attained were not very accurate due to the presence of two-magnon scattering and exchange coupling, which did not cause the α values to systematically increase or decrease but did affect their accuracy.

Bibliography

[1] S. V. Vonsovskii, *Ferromagnetic Resonance: The Phenomenon of Resonant Absorption of a High-Frequency Magnetic Field in Ferromagnetic Substances*, Pergamon, (1966).

[2] J. H. E. Griffiths, *Anomalous High-Frequency Resistance of Ferromagnetic Metals*, Nature 158, 670-671, (1946).

[3] Charles Kittel, *Ferromagnetic resonance*, J. Phys. Radium, 1951, 12 (3), pp.291-302, (1951).

[4] O. Acher, S. Dubourg, *A generalization of Snoek's law to ferromagnetic films and composites*, Phys. Rev. B 77, 104440, (2007).

[5] Nguyen N. Phuoc, H. Y. Chen, C. K. Ong *Effect of antiferromagnetic thickness on thermal stability of static and dynamic magnetization of NiFe/FeMn multilayers*, Journal of Applied Physics 113, 063913, (2013).

[6] L. Berger, *Emission of spin waves by a magnetic multilayer traversed by a current*, Phys. Rev. B 54, 9353, (1996).

[7] J. C. Slonczewski, *Current-driven excitation of magnetic multilayers* , J. Magn. Magn. Mater. 159, L1, (1996).

[8] Xiaoxi Zhong, Wee Tee Soh, Nguyen N. Phuoc, Ying Liu, C. K. Ong, *Multiple resonance peaks of FeCo thin films with NiFe underlayer*, Journal of Applied Physics 117, 013906, (2015).

[9] N. X. Sun, S. X. Wang, *Soft magnetism of FeCoN thin films with a Permalloy underlayer*, Journal of Applied Physics 92, 1477, (2002).

[10] Mingzhong Wu, *Damping in Present Magnetic Recording Media*, Department of Physics, Colorado State University, (2011).

[11] Matthias Wuttig, Xiangdong Liu, *Ultrathin Metal Films: Magnetic and Structural Properties*, Springer Berlin Heidelberg, (2004).

[12] David M. Pozar, *Microwave Engineering*, John Wiley & Sons, Inc. 56-103 & 497-511, (1998).

[13] R. L. Rodriguez-Suarez, L. H. Vilela-Leao, T. Bueno, A. B. Oliveira, J. R. L. de Almeida, P. Landeros, S. M. Rezende, A. Azevedo, *Critical thickness investigation of magnetic properties in exchange-coupled bilayers*, Phys. Rev. B 83,224418, (1996).

[14] Charles Kittel, *Introduction to Solid State Physics*, Wiley, 8th Edition. (2005).

[15] L. Landau and E. Lifshits, *On the Theory of the Dispersion of Magnetic Permeability in Ferromagnetic Bodies*, Phys. Z. Sowjetunion 8, 153, (1935).

[16] T. L. Gilbert, *A phenomenological theory of damping in ferromagnetic materials*, IEEE Trans. Magn. 40, 3443, (2004).

[17] Juretschke, *dc Detection of Spin Resonance in Thin Metallic Films*, J. Appl. Phys., 34, 1223, (1963).

[18] D.L. Mills, Rodrigo Arias, *Critical thickness investigation of magnetic properties in exchange-coupled bilayers*, Top. Appl. Phys. 87, 27, (2003).

[19] P. Landeros, Rodrigo Arias, D.L. Mills, *Two magnon scattering in ultrathin ferromagnets: The case where the magnetization is out of plane*, Phys. Rev. B 77, 214405, (2008).

[20] K. Zakeri, J. Lindner, I. Barsukov, R. Meckenstock, M. Farle, U. von Horsten, H. Wende, W. Keune, J. Rocker, S. S. Kalarickal, K. Lenz, W. Kuch, K. Baberschke, and Z. Frait, *Two magnon scattering in ultrathin ferromagnets: The case where the magnetization is out of plane*, Phys. Rev. B 76, 104416, (2007).

[21] R. D. McMichael, D. J. Twisselmann, and A. Kunz, *Localized Ferromagnetic Resonance in Inhomogeneous Thin Films*, Phys. Rev. Lett. 90, 227601, (2003).

[22] J. Nogues, Ivan K. Schuller, *Exchange Bias*, Journal of Magnetism and Magnetic Materials, 192, (1999).

[23] Joachim Stohr, Hans Christoph Siegmann, *Magnetism: From Fundamentals to Nanoscale Dynamics*, Springer-Verlag Berlin Heidelberg, (2006).

[24] M. D. Stiles, R. D. McMichael, *Model for exchange bias in polycrystalline ferromagnet-antiferromagnet bilayers*, Phys. Rev. B 58, (1998).

[25] Nie, H.B., Xu, S.Y., Ong, C.K., Zhan, Q., Li, D.X., Wang, J.P., *In-plane magnetic anisotropy in RF sputtered Fe-N thin films*, ScholarBank@NUS, (2003).

[26] Xiaoxi Zhong, Nguyen N. Phuoc, Ying Liu, C.K. Ong, *Employment of Co underlayer and oblique deposition to obtain high resonance frequency and excellent thermal stability in FeCo thin films*, Journal of Magnetism and Magnetic Materials 365, (2014).

[27] V. Bekker, K. Seemann, and H. Leiste, *A new strip line broad-band measurement evaluation for determining the complex permeability of thin ferromagnetic films* J. Magn. Magn. Mater. 270, 327, (2004).

[28] H. J. Juretschke, *Electromagnetic Theory of dc Effects in Ferromagnetic Resonance* J. Appl. Phys. 31, 1401 (1960).

[29] Wee Tee Soh, Bin Peng, Guozhi Chai, C. K. Ong, *Electrical detection and quantification of spin rectification effect enabled by shorted microstrip transmission line technique*, Review of Scientific Instruments 85, 026109, (2014).

[30] Y. Liu, L. Chen, C. Y. Tan, H. J. Liu, and C. K. Ong, *Broadband complex permeability characterization of magnetic thin films using shorted microstrip transmission-line perturbation*, Review of Scientific Instruments 76, 063911, (2005).

[31] Hang Chen, Xiaolong Fan, Wenxi Wang, Hengan Zhou, Y. S. Gui et al., *Electric detection of the thickness dependent damping in Co90Zr10 thin films*, Appl. Phys. Lett. 102, 202410, (2013).

[32] J. Geshev, S. Nicolodi, R. B. da Silva, J. Nogues, V. Skumryev, M. D. Baro, *Discrimination between coupling and anisotropy fields in exchange-biased layers* J. Appl. Phys. 105, 053903, (2009).

[33] J. Wu, J. S. Park, W. Kim, E. Arenholz, M. Liberati, A. Scholl, Y. Z. Wu, Chanyong Hwang, and Z. Q. Qiu, *Direct Measurement of Rotatable and Frozen CoO Spins in Exchange Bias System of CoO/Fe/Ag(001)*, Phys. Rev. Lett. 104, 217204, (2010).

[34] Gui YongSheng, Bai LiHui, Hu CanMing, *The Physics of Spin Rectification Effect and its Application*, Science China 56, (2012).

[35] Siddharth Rao, Sankha Subhra Mukherjee, Mehrdad Elyasi, Charanjit Singh Bhatia, Hyunsoo Yang, *Electrical detection of microwave assisted magnetization reversal by spin pumping*, Applied Physics Letters 104, 122406, (2014).

[36] Hua Chen, Qian Niu, A. H. MacDonald, *Anomalous Hall Effect Arising from Noncollinear Antiferromagnetism*, Phys. Rev. Lett. 112, 017205, (2014).

[37] K. Ando, S. Takahashi, J. Ieda, Y. Kajiwara, H. Nakayama, T. Yoshino, K. Harii, Y. Fujikawa, M. Matsuo, S.Maekawa, E. Saitoh, *Inverse spin-Hall effect induced by spin pumping in metallic system*, Journal of Applied Physics 109, 103913, (2011).